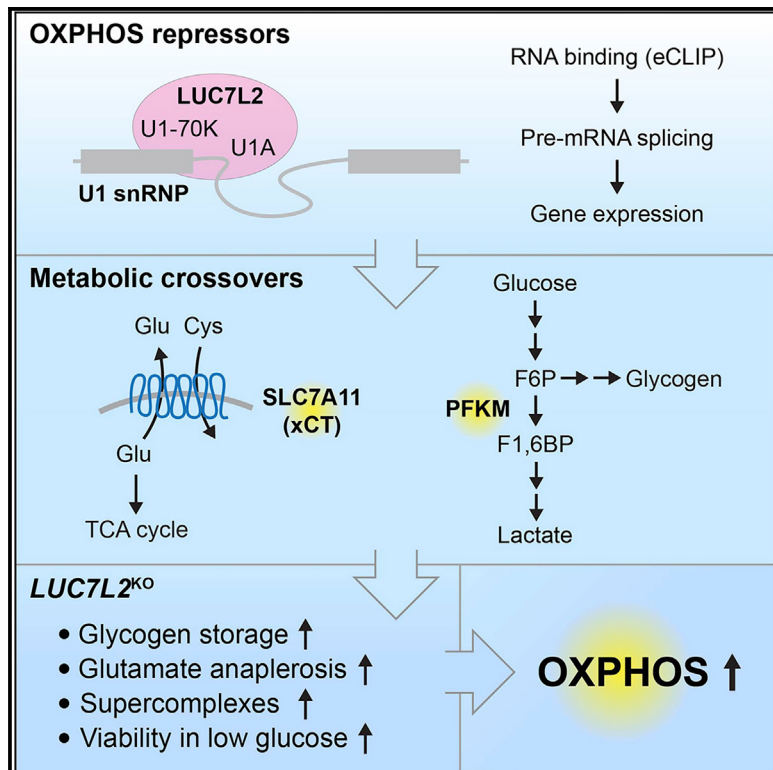


## Loss of *LUC7L2* and U1 snRNP subunits shifts energy metabolism from glycolysis to OXPHOS

### Graphical abstract



### Authors

Alexis A. Jourdain, Bridget E. Begg,  
Eran Mick, ..., Gene W. Yeo,  
Christopher B. Burge, Vamsi K. Mootha

### Correspondence

alexis.jourdain@unil.ch (A.A.J.),  
vamsi@hms.harvard.edu (V.K.M.)

### In brief

Jourdain et al. report the identification of OXPHOS repressors, genes whose loss shifts metabolism from glycolysis to OXPHOS. Prominent in this set are members of the U1 snRNP, including *LUC7L2*. The authors show that loss of *LUC7L2* leads to metabolic crossovers at *PFKM* and *SLC7A11* (xCT), thereby impacting glycogen formation and glutamate oxidation.

### Highlights

- Expression of *LUC7L2* and the U1 snRNP represses OXPHOS
- Pre-mRNA splicing and expression of *PFKM* and *SLC7A11* (xCT) requires *LUC7L2*
- Loss of *LUC7L2* and glycolysis promotes respiratory chain (super)complex assembly
- LUC7* family members cross-regulate each other's expression

## Article

# Loss of *LUC7L2* and U1 snRNP subunits shifts energy metabolism from glycolysis to OXPHOS

Alexis A. Jourdain,<sup>1,2,3,6,\*</sup> Bridget E. Begg,<sup>4</sup> Eran Mick,<sup>1,2,3,7</sup> Hardik Shah,<sup>1,2,3</sup> Sarah E. Calvo,<sup>1,2,3</sup> Owen S. Skinner,<sup>1,2,3</sup> Rohit Sharma,<sup>1,2,3</sup> Steven M. Blue,<sup>5</sup> Gene W. Yeo,<sup>5</sup> Christopher B. Burge,<sup>4</sup> and Vamsi K. Mootha<sup>1,2,3,8,\*</sup>

<sup>1</sup>Department of Molecular Biology and Howard Hughes Medical Institute, Massachusetts General Hospital, Boston, MA 02114, USA

<sup>2</sup>Department of Systems Biology, Harvard Medical School, Boston, MA 02115, USA

<sup>3</sup>Broad Institute of MIT and Harvard, Cambridge, MA 02142, USA

<sup>4</sup>Department of Biology, MIT, Cambridge, MA 02139, USA

<sup>5</sup>Department of Cellular and Molecular Medicine, Institute for Genomic Medicine, University of California, San Diego, La Jolla, CA 92093, USA

<sup>6</sup>Present address: Department of Biochemistry, University of Lausanne, Epalinges 1066, Switzerland

<sup>7</sup>Present address: Division of Infectious Diseases & Division of Pulmonary and Critical Care Medicine, University of California, San Francisco, San Francisco, CA 94143, USA

<sup>8</sup>Lead contact

\*Correspondence: [alexis.jourdain@unil.ch](mailto:alexis.jourdain@unil.ch) (A.A.J.), [vamsi@hms.harvard.edu](mailto:vamsi@hms.harvard.edu) (V.K.M.)

<https://doi.org/10.1016/j.molcel.2021.02.033>

## SUMMARY

Oxidative phosphorylation (OXPHOS) and glycolysis are the two major pathways for ATP production. The reliance on each varies across tissues and cell states, and can influence susceptibility to disease. At present, the full set of molecular mechanisms governing the relative expression and balance of these two pathways is unknown. Here, we focus on genes whose loss leads to an increase in OXPHOS activity. Unexpectedly, this class of genes is enriched for components of the pre-mRNA splicing machinery, in particular for subunits of the U1 snRNP. Among them, we show that *LUC7L2* represses OXPHOS and promotes glycolysis by multiple mechanisms, including (1) splicing of the glycolytic enzyme *PFKM* to suppress glycogen synthesis, (2) splicing of the cystine/glutamate antiporter *SLC7A11* (*xCT*) to suppress glutamate oxidation, and (3) secondary repression of mitochondrial respiratory supercomplex formation. Our results connect *LUC7L2* expression and, more generally, the U1 snRNP to cellular energy metabolism.

## INTRODUCTION

Human cells use two chief pathways for generating ATP: glycolysis and oxidative phosphorylation (OXPHOS) (Figure 1A). Use of these metabolic routes is associated with key tradeoffs, and while glycolysis tends to be kinetically favorable, the ATP yield from OXPHOS is higher (Pfeiffer et al., 2001). The relative balance of OXPHOS and glycolysis varies across tissues. For example, while cardiac tissue is rich in mitochondria and highly oxidative in its metabolism, proliferating cells from the thymus are highly glycolytic (Warburg, 1924). Balance between these two programs can vary during cellular differentiation and in response to environmental stimuli. The activation of immune cells is often accompanied by rewiring toward glycolysis, while stem cell differentiation results in increased OXPHOS (Pearce et al., 2013; Ito and Suda, 2014). Cells also acutely respond to nutrient and oxygen availability to adjust flux through these pathways within minutes (Crabtree, 1929; Pasteur, 1861), while oncogenic transformation promotes aerobic glycolysis (Warburg, 1924). Notably, differential reliance on OXPHOS versus glycolysis can be exploited for therapeutic benefit (Bonnet et al., 2007; Gohil et al., 2010).

A small number of genomic programs have been identified that can influence the balance of cellular energy metabolism. For example, the transcriptional co-activator peroxisome proliferator-activated receptor-gamma coactivator-1 $\alpha$  (PGC-1 $\alpha$ ) integrates nutrient levels and physiological inputs to orchestrate a genomic program that induces the expression of the OXPHOS machinery (Puigserver et al., 1998). Conversely, the transcription factor hypoxia-inducible factor-1 $\alpha$  (HIF-1 $\alpha$ ) promotes expression of a set of genes, including glycolytic enzymes, in response to a decline in oxygen levels (Huang et al., 1998). Post-transcriptionally, RNA-binding proteins such as clustered mitochondria homolog (CLUH) bind to a large number of mRNAs encoding mitochondrial proteins (Gao et al., 2014). A few instances of alternative splicing regulating individual metabolic enzymes have also been reported. For example, alternative splicing to generate the pyruvate kinase M2 (PKM2) isoform of the pyruvate kinase, promoting glycolytic carbon flux, is believed to contribute to cancer progression (Christofk et al., 2008).

High-throughput approaches can provide insight into the regulation and patterning of cellular metabolic programs (Hillenmeyer et al., 2008; VanderSluis et al., 2014). We previously reported a nutrient-sensitized screen for small molecules that

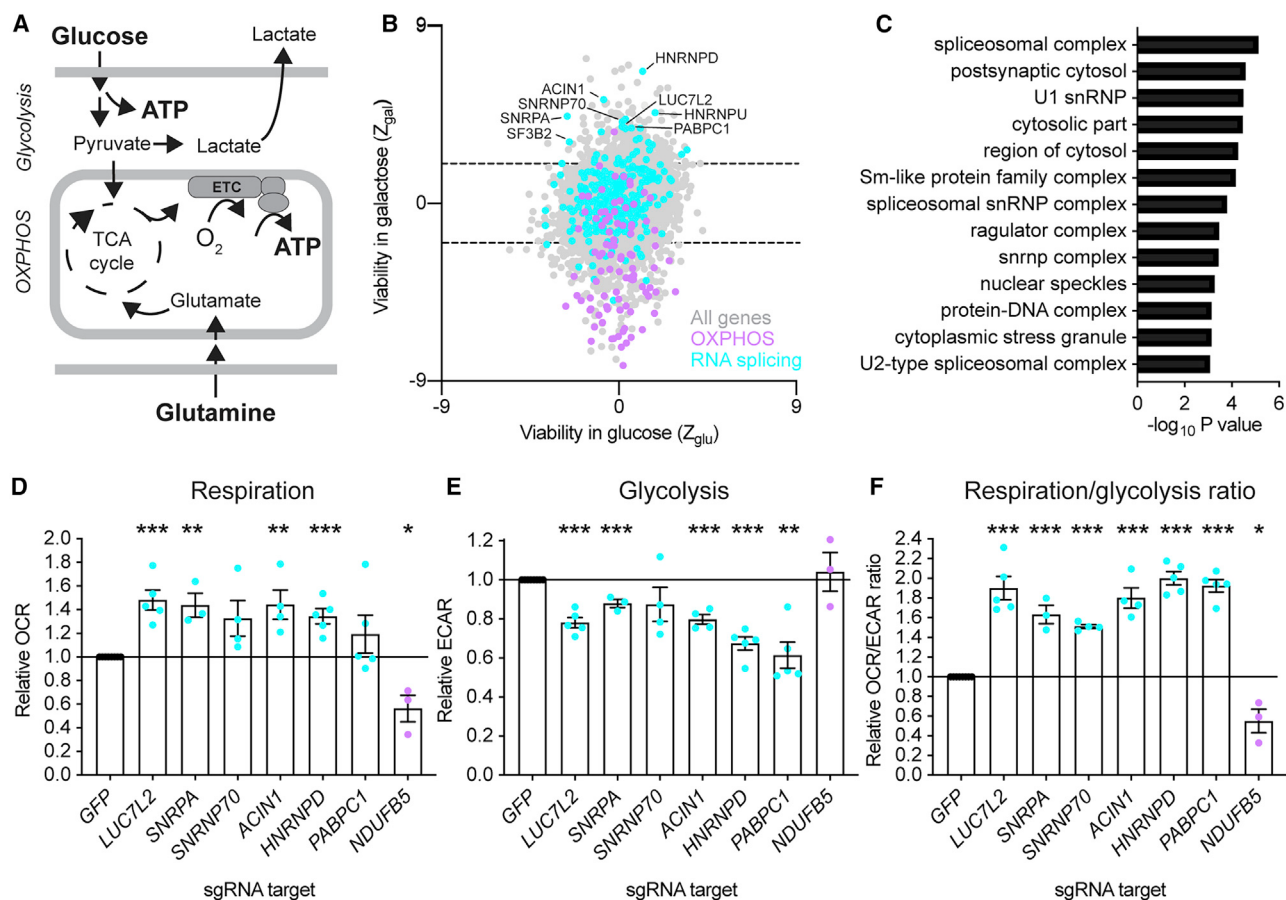


**Figure 1. Identification of pre-mRNA splicing components as repressors of OXPHOS**

(A) Overview of the main ATP-generating pathways in human cells. ETC, electron transport chain; OXPHOS, oxidative phosphorylation; TCA, tricarboxylic acid cycle.  
 (B) Gene-level analysis of a genome-wide CRISPR/Cas9 screen in glucose and galactose. Each dot represents an expressed, non-essential gene (n = 9,189).  
 (C) Gene Ontology (GO) analysis generated using a gene list ranked by viability in galactose against GO components.  
 (D–F) Functional validation of the screening results. Basal whole-cell oxygen consumption rates (OCRs), extracellular acidification rates (ECARs), and OCR:ECAR ratios were simultaneously measured after CRISPR/Cas9-mediated gene depletion in K562 cells grown in glucose-containing media.  
 All data are shown as means ± SEMs. n ≥ 3 independent experiments. \*p < 0.05, \*\*p < 0.01, and \*\*\*p < 0.001, t test relative to control (GFP) sgRNA-treated cells. NDUFB5 is a control with a known role in OXPHOS.  
 See also Figure S1 and Table S1.

affect the fitness of cells in galactose, a poor substrate for glycolysis, and focused on dozens of small molecules that induce a shift from OXPHOS to glycolysis (Gohil et al., 2010). Recently, we reported the genome-wide identification of genes necessary to sustain OXPHOS (Arroyo et al., 2016). We systematically catalogued genes whose loss impaired OXPHOS in human cells, including 72 that underlie known OXPHOS diseases. However, that report did not explore the opposite side of the screen, which could in principle include pathways that tonically suppress OXPHOS.

Here, we report the genome-wide identification of “OXPHOS repressors,” defined as genes whose knockout (KO) promotes relative fitness in the absence of glucose as a fuel for glycolysis. We validate top-scoring genes and show that their depletion augments OXPHOS activity. OXPHOS repressors are enriched for components of the pre-mRNA splicing machinery, including

subunits of the U1 small nuclear ribonucleoprotein (snRNP). Among them, we show that *LUC7L2* encodes a U1 snRNP subunit involved in pre-mRNA splicing and gene expression. Among *LUC7L2* gene targets, we focus on 2 genes, *PFKM* and *SLC7A11* (xCT), which we show represent 2 metabolic crossovers that influence the bioenergetic state of the cell in a *LUC7L2*-dependent manner.

## RESULTS

### Genome-wide search for factors that limit OXPHOS identifies components of the pre-mRNA splicing machinery

To nominate genes whose deletion promotes OXPHOS, we re-analyzed the results of our genome-wide “death screen” that compared the viability of CRISPR/Cas9 mutagenized K562 cells

that are shifted to glucose or galactose conditions for 24 h (Arroyo et al., 2016). The loss of genes required for OXPHOS is tolerated in the presence of glucose, whereas these genes are conditionally essential in galactose, as it is a poor substrate for glycolysis (Robinson et al., 1992). We reanalyzed 9,189 expressed non-essential genes in K562 cells, calculating a Z score of viability of the gene KO under each condition (Figure 1B; Table S1). In this analysis, single guide RNAs (sgRNAs) targeting 3,726 unexpressed genes were used as negative controls. Gene Ontology (GO) analysis confirmed our previous result, that the depletion of genes encoding subunits of the mitochondrial respiratory chain (RC) caused the loss of viability, as expected (Figure S1A).

Unexpectedly, the genes whose depletion promotes relative viability in galactose were enriched in splicing-related GO terms, including “spliceosomal complex” ( $p < 10^{-5}$ ) and “U1 snRNP” ( $p < 10^{-4}$ ) (Figures 1C and S1B). Hits with these GO terms included U1 snRNP-specific subunits (*LUC7L2*, *SNRPA*, *SNRNP70*), heterogeneous nuclear ribonucleoproteins (*HNRNPD*, *HNRNPU*), splicing factors (*SF3B2*, *SFPQ*), RNA helicases (*DHX8*, *DDX47*), an LSm-family protein (*LSM1*), an exon junction complex protein (*ACIN1*), and a polyadenylate-binding protein (*PABPC1*). Other gene expression pathways were not significantly enriched.

We used CRISPR/Cas9 and sgRNA sequences from the screening library to disrupt the expression of 6 representative genes identified in the screen that were not previously linked to energy metabolism, including *LUC7L2*, *SNRPA* (U1A), *SNRNP70* (U1-70K), *ACIN1*, *HNRNPD*, and *PABPC1*. We included a gene encoding a subunit of respiratory complex I (*NDUFB5*) as a control with known impact on metabolism, and measured oxygen consumption rates (OCRs), a proxy for OXPHOS, and extracellular acidification rates (ECARs), a proxy for glycolysis, in transduced K562 cells. Notably, depletion of several of these genes significantly increased basal, maximal and ATP-linked OCR (Figures 1D, S1C, and S1D), while also decreasing ECAR (Figure 1E), suggesting rewiring of metabolism from glycolysis to OXPHOS. In fact, the OCR:ECAR ratios were significantly increased upon depletion of all six selected genes (Figure 1F), whereas it decreased in *NDUFB5*-depleted cells, as expected. Together, these results confirm that silencing certain pre-mRNA splicing genes boosts oxidative energy metabolism.

### Expression of *LUC7L2* represses OXPHOS

Among the validated screening hits, *LUC7L2* showed the most robust phenotype. This relatively unstudied gene belongs to the LUC7 family together with *LUC7L* and *LUC7L3*, all of which are homologs of yeast *LUC7*, a U1 snRNP protein involved in pre-mRNA splicing (Fortes et al., 1999). Mutations, haploinsufficiency, and complete loss of *LUC7L2* are associated with poorer survival in myelodysplastic syndromes (MDSs) (Singh et al., 2013), while *Arabidopsis LUC7* genes contribute to development and stress responses (de Francisco Amorim et al., 2018). None of the LUC7 family members have been previously linked to energy metabolism.

To further investigate the function of *LUC7L2*, we used CRISPR/Cas9 to generate single-cell clones in which the expression of *LUC7L2* was ablated (Figures S2A–S2C). We observed

that *LUC7L2*<sup>KO</sup> K562 cells grew more slowly relative to wild type (WT) in standard 25 mM glucose cell culture conditions (Figure 2A). However, they grew comparatively faster than *LUC7L2*<sup>WT</sup> cells when glycolysis was limiting, either pharmacologically by treatment with 2-deoxyglucose (2-DG) or when glucose was replaced by galactose (Figure 2B). In contrast, *LUC7L2* depletion sensitized cells to killing by the pharmacologic inhibition of OXPHOS (Figure 2C).

Next, we characterized the bioenergetic consequences of *LUC7L2* depletion. OCR measurement confirmed our initial observation that *LUC7L2* represses OXPHOS, and, accordingly, all measured respiratory parameters in *LUC7L2*<sup>KO</sup> K562 and HAP1 cells were increased relative to controls (Figures 2D and S2D–S2F). As expected from our initial validation, *LUC7L2*-depleted K562 clones exhibited less ECAR (Figure 2E). To test whether the global abundance of mitochondria was affected by *LUC7L2* depletion, we quantified mitochondrial DNA copy number and citrate synthase activity and observed no differences (Figures 2F and 2G). Electron microscopy also confirmed the absence of gross differences in mitochondrial abundance or ultrastructure in these cells (Figure S2G). Our results indicate that *LUC7L2* affects metabolic state-dependent cell growth and bioenergetics. While *LUC7L2* loss does not appear to affect the gross abundance of mitochondria, it influences the balance between the activity of glycolysis and OXPHOS.

### Metabolic basis of the shift from glycolysis to OXPHOS in *LUC7L2*-depleted cells

The rewiring of cellular bioenergetics upon *LUC7L2* depletion prompted us to analyze the abundance of metabolic intermediates central to glycolysis and OXPHOS. We used liquid chromatography-mass spectrometry (LC-MS) to quantify the relative steady-state levels of 122 metabolites in cell pellets as well as the absolute consumption/release rates of 22 media metabolites (Tables S2 and S3). Consistent with our ECAR results, we observed reduced rates of glucose uptake, lactate secretion, and media acidification, as well as a dramatically decreased media lactate:pyruvate ratio in *LUC7L2*<sup>KO</sup> K562 cells, all consistent with decreased glycolysis (Figures 3A–3C, S3C, and S3F). In pellets of *LUC7L2*<sup>KO</sup>, we observed the significant accumulation of glucose, glucose-6-phosphate, and fructose-6-phosphate/glucose-1-phosphate isomers. Notably, levels of fructose-1,6-bisphosphate, the fourth intermediate of glycolysis and the product of phosphofructokinase (PFK), were significantly reduced in the absence of *LUC7L2*. Thus, we observed the accumulation of the substrate of PFK and the depletion of its product, identifying this enzyme as a metabolic crossover in *LUC7L2*<sup>KO</sup> cells. A loss of function mutation in *PFKM* leads to skeletal muscle glycogen accumulation (Tarui et al., 1965), and we observed significant accumulation of glycogen and its precursor uridine diphosphate (UDP) glucose in *LUC7L2*<sup>KO</sup> cells (Figure 3A).

Our metabolite analysis also provided insight into how mitochondrial metabolism is rewired in *LUC7L2*<sup>KO</sup> cells. We observed accumulation of 4 of the 5 TCA metabolites analyzed (2-ketoglutarate, succinate, fumarate, malate) as well as two tricarboxylic acid (TCA) cycle-derived metabolites (2-hydroxyglutarate, aspartate) (Figures 3A and S3A). Glutamine is an important fuel that can contribute glutamate to the TCA cycle

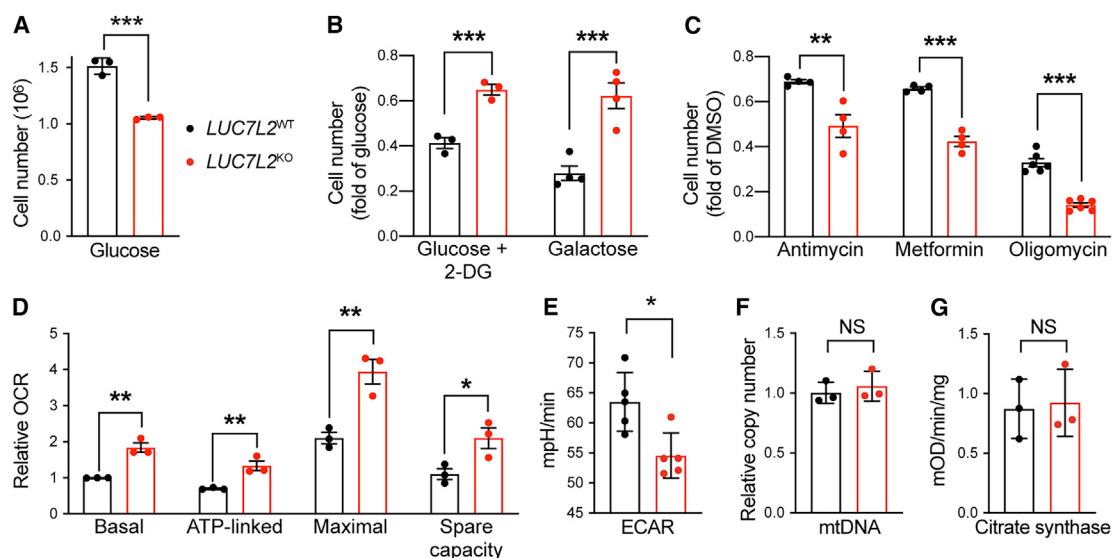


**Figure 2. LUC7L2 affects metabolic state-dependent cell growth and bioenergetics**

(A–C) Cell proliferation of LUC7L2<sup>KO</sup> K562 cells grown in (A) glucose and (B) treated with 2-deoxyglucose (2-DG) or when glucose was replaced by galactose or (C) glucose with OXPHOS inhibitors.

(D) Respiratory parameters of LUC7L2<sup>KO</sup> cells as determined by OCR.

(E) Basal glycolytic activity in LUC7L2<sup>KO</sup> cells as determined by ECAR.

(F and G) Relative mtDNA abundance (F) and (G) citrate synthase activity of LUC7L2<sup>KO</sup> cells.

All data are shown as means  $\pm$  SEMs ( $n \geq 3$ ). \* $p < 0.05$ , \*\* $p < 0.01$ , and \*\*\* $p < 0.001$ , t test relative to LUC7L2<sup>WT</sup> cells.

See also Figure S2.

(Reitzer et al., 1979), but glutamine consumption and intracellular glutamine levels remained unchanged (Figures 3A and 3B). In contrast, intracellular glutamate accumulated in LUC7L2<sup>KO</sup> cells. Intracellular glutamate may either be converted into 2-ketoglutarate to serve as an anaplerotic input into the TCA cycle or be exported out of the cell in exchange for cystine via the system X<sub>c</sub><sup>-</sup>, a plasma membrane antiporter encoded by 2 subunits, SLC7A11 (xCT) and SLC3A2 (4F2) (Sato et al., 1999). The system X<sub>c</sub><sup>-</sup> has previously been implicated in the survival of cells in low glucose conditions (Shin et al., 2017; Koppula et al., 2017). Importantly, we found that while intracellular glutamate accumulated in LUC7L2-depleted cells, its secretion to the culture media was significantly reduced (Figure 3B). These observations pointed to a second crossover at the level of the system X<sub>c</sub><sup>-</sup>, as LUC7L2-depleted cells also consumed less media cystine (Figures 3B and S3E).

Collectively, analysis of steady-state intracellular metabolites, as well as consumption and release of media metabolites, indicate that the loss of LUC7L2 modulates 2 key crossovers in energy metabolism: (1) upper glycolysis/glycogen storage at PFK, and (2) glutamate oxidation/secretion via the exchange of cystine and glutamate at the transporter system X<sub>c</sub><sup>-</sup>. The direction of these metabolic changes is concordant with the observed shift from glycolysis to OXPHOS in cells lacking LUC7L2.

#### LUC7L2 is a U1 snRNP subunit involved in pre-mRNA splicing

Next, we sought to determine how the loss of LUC7L2 leads to the remodeling of cellular energy metabolism. LUC7L2 is not a

well-studied gene, but its yeast and plant homologs encode components of the U1 snRNP. Hence, we predicted that LUC7L2 is a component of the mammalian snRNP, affecting the splicing and expression of genes that may be influencing energy metabolism.

We used confocal microscopy to confirm the nuclear localization of LUC7L2 and observed that it localized in SRSF2<sup>+</sup> nuclear speckles, which are themselves enriched for the pre-mRNA splicing machinery (Rino et al., 2007; Figure 4A). We next immunoprecipitated LUC7L2 and discovered 29 interacting proteins using MS, including our validated screening hits SNRPA and SNRNP70 and most other known U1 subunits (Figures 4B and 4C; Table S4).

We next sought to identify the transcripts that are bound by endogenous LUC7L2 and used enhanced crosslinking and immunoprecipitation (eCLIP) coupled to RNA deep-sequencing (Van Nostrand et al., 2016). In agreement with the proposed role for LUC7L2 as a U1 snRNP subunit, we found that LUC7L2 crosslinks to the U1 snRNA, and to a lesser extent to the U6 snRNA, which comes in close proximity during the transfer of the 5' splice site (5'SS) during spliceosome assembly (Plaschka et al., 2018; Figure 4D). We identified eCLIP peaks for LUC7L2 in 5,595 genes in HeLa cells and 3,378 genes in K562 cells. Of these, 2,614 were shared (expression-corrected overlap significance  $p < 10^{-3}$ , Poisson) (Figure 4E; Table S5). Within pre-mRNAs, we found that LUC7L2 bound mainly to exons and introns (Figure 4F). A meta-analysis revealed that LUC7L2 preferentially bound near SSs (Figure 4G). The pattern of binding near SSs is consistent with the association of LUC7L2 with U1 snRNP complexes, which recognize 5'SS

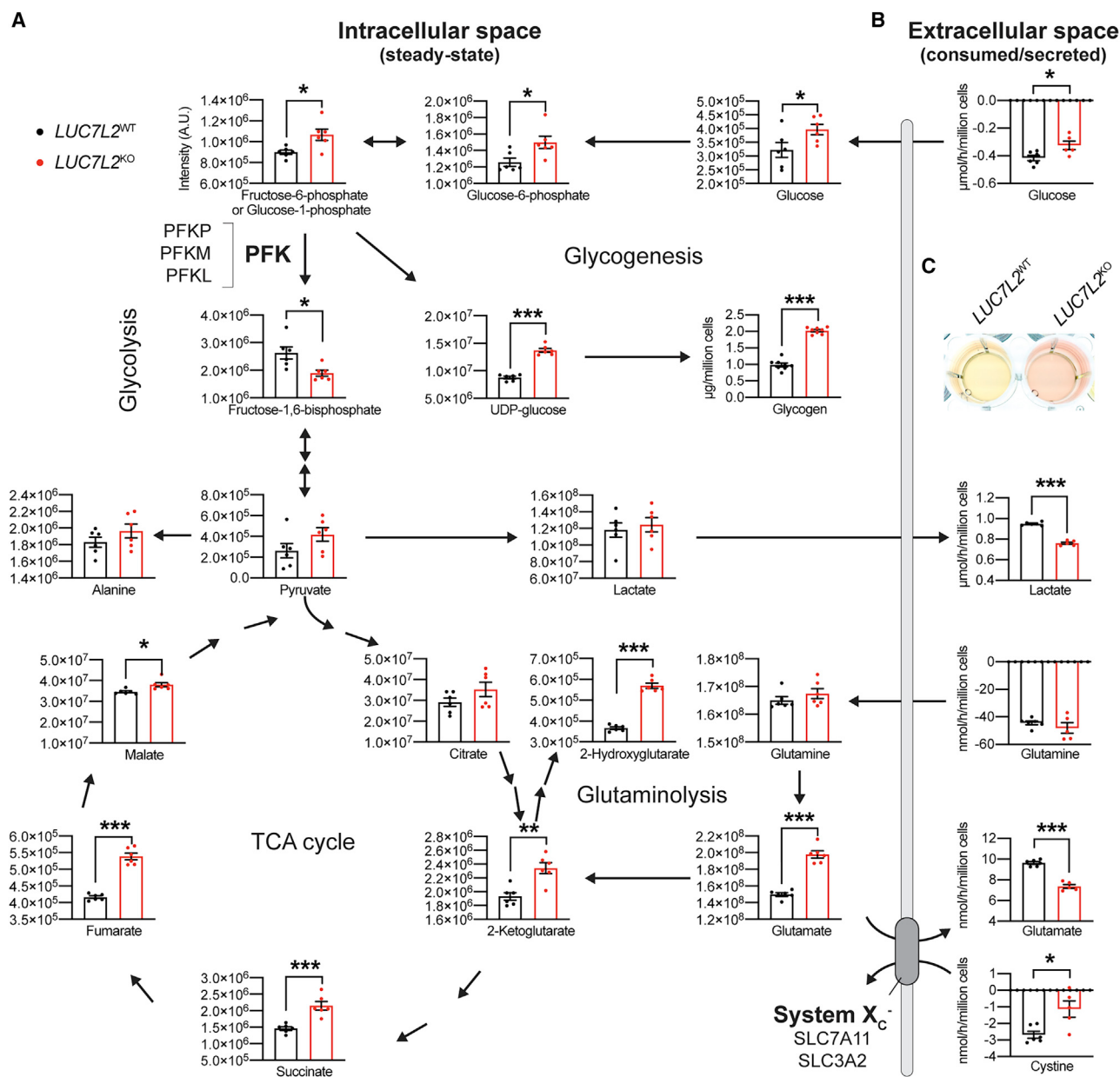


**Figure 3. Metabolite analysis in *LUC7L2*-depleted cells reveals crossovers at phosphofructokinase and system X<sub>c</sub><sup>-</sup>**

(A) Intracellular levels of metabolites in *LUC7L2<sup>KO</sup>* K562 cells as determined by LC-MS.

(B) Extracellular levels of metabolites as determined by LC-MS analysis of the spent media from (A). Positive and negative values illustrate metabolite secretion and consumption by the cells, respectively.

(C) Media acidification of *LUC7L2<sup>KO</sup>* K562 cells grown in glucose.

All data are shown as means ± SEMs (n = 5–8). \*p < 0.05, \*\*p < 0.01, and \*\*\*p < 0.001, t test relative to *LUC7L2<sup>WT</sup>*.

See also Figure S3 and Tables S2 and S3.

motifs and also interact with U2 snRNP bound upstream of 3'SSs (De Conti et al., 2013)

To understand the impact of *LUC7L2<sup>KO</sup>* on gene expression, we profiled the transcriptomes of *LUC7L2<sup>KO</sup>* HeLa and K562 cells. Loss of *LUC7L2* changed the expression of ~1,000–1,500 genes in each cell type (false discovery rate [FDR] < 10<sup>-4</sup> and >50% absolute fold change), 149 of which were shared

(overlap not significant) (Figures 4H and S4; Table S6). Splicing analysis using rMATs (Shen et al., 2014) identified 4,815 and 4,704 alternative splicing events in HeLa and K562 cells, respectively (FDR < 0.1 and |Δψ| > 0.05, where ψ represents “percent spliced in” and Δψ is the change in ψ following gene depletion) (Figure 4I; Table S7). In all, 485 splicing changes were shared between both cell types (expression-corrected overlap significance

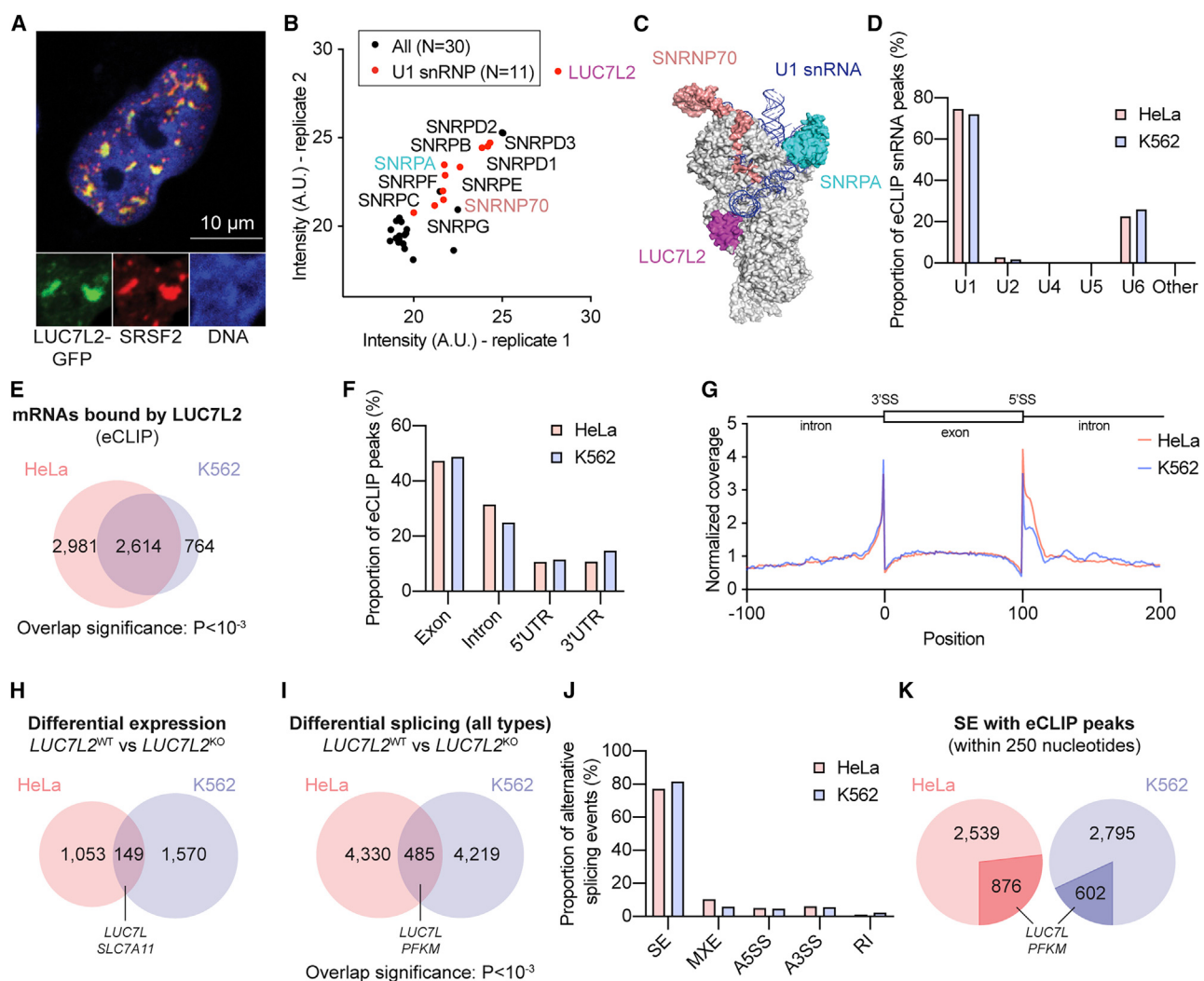


**Figure 4. *LUC7L2* encodes a U1 snRNP subunit involved in pre-mRNA splicing**

- (A) Confocal microscopy of a single nucleus from a HeLa cell expressing LUC7L2-GFP and immunolabeled with antibodies to SRSF2.
  - (B) LUC7L2-interacting proteins as determined by IP-MS ( $n = 2$ ).
  - (C) Representation of LUC7L2 (LUC7), SNRPA (U1-A), and SNRNP70 (U1-70K) on the yeast U1 snRNP (PDB: 5UZ5) (Li et al., 2017).
  - (D) Proportion of eCLIP peaks mapping to splicing snRNAs in HeLa and K562 cells (eCLIP,  $n = 2$  each).
  - (E) Representation of the genes bound by LUC7L2 at  $p < 10^{-4}$ .
  - (F) Proportion of LUC7L2 eCLIP peaks in pre-mRNAs at  $p < 10^{-4}$ .
  - (G) Meta-analysis of LUC7L2 binding sites across shared eCLIP peaks at  $p < 10^{-4}$ .
  - (H) Differential gene expression in *LUC7L2*<sup>KO</sup> cells ( $n = 3$  for each cell type and each genotype) as determined by RNA deep sequencing at FDR  $< 10^{-4}$  and  $> |1.5|$ -fold change.
  - (I) Alternative splicing events seen in *LUC7L2*<sup>KO</sup> cells as determined by rMATS at FDR  $< 0.1$  and  $|\Delta\psi| > 0.05$  ( $n = 3$  for each cell type and each genotype).
  - (J) Types of alternative splicing in *LUC7L2*<sup>KO</sup> cells with SE. A3SS, alternative 3' splice site; A5SS, alternative 5' splice site; MXEs, mutually exclusive exons; RI, retained intron; SE, skipped exon.
  - (K) Alternative events presenting an eCLIP peak at a 250-nt distance from splicing events at  $p < 10^{-2}$  (darker shading).
- See also Figure S4 and Tables S4, S5, S6, and S7.

$p < 10^{-3}$ , Poisson) (Figure 4I). Skipped exons (SEs) comprised the majority of *LUC7L2*-induced alternative splicing events (Figure 4J), and ~20%–25% of these splicing events had a *LUC7L2* binding site within a distance of 250 nt from a SS (Figure 4K). The binding of *LUC7L2* in close proximity to a SE event supports a direct effect of *LUC7L2* on these exons, although the absence

of an adjacent CLIP peak does not imply that regulation is not direct, since CLIP does not detect all binding, and some regulation may occur across longer distances (Lovci et al., 2013; Van Nostrand et al., 2020).

Our RNA sequencing (RNA-seq) and eCLIP analyses indicate that *LUC7L2* affects pre-mRNA splicing and gene expression.

# Molecular Cell

## Article

Importantly, among the genes most significantly affected in the splicing analysis was *PFKM* (Figure 4I), and among the most differentially expressed genes was *SLC7A11* (Figure 4H). Both of these correspond to the metabolic crossovers identified above (Figure 3). We next sought to validate these splicing and gene expression changes as being downstream of *LUC7L2* to determine whether they may contribute to the observed metabolic phenotype.

### ***LUC7L2* promotes expression of *PFKM* and suppresses glycogen storage**

We investigated the changes in *PFKM* and other glycolytic enzymes following *LUC7L2* depletion. Most transcripts encoding glycolytic enzymes were bound by *LUC7L2* in eCLIP ( $FDR < 10^{-4}$ ), and we found alternative splicing in *PFKM*, *PKM*, *ALDOA*, and *ENO3* ( $FDR < 0.1$ , Tables S5 and S7). Of all glycolytic enzymes, *PFKM* was the most significantly alternatively spliced in both *LUC7L2*<sup>KO</sup> HeLa and K562 cells, with 2 altered splicing events detected: increased usage of an alternative 5'SS between exons 11 and 12 ( $\Delta\psi = 0.29$ ,  $FDR < 10^{-11}$ ) and exon 12 skipping ( $\Delta\psi = -0.19$ ,  $FDR < 10^{-12}$ ). *LUC7L2* binding was observed near the 5'SS of both alternatively spliced exons (Figure 5A). Notably, our unbiased metabolomics experiment suggested decreased *PFKM* activity in *LUC7L2*<sup>KO</sup> cells (Figure 3A), and both alternative splicing events were expected to reduce *PFKM* activity. First, the alternative 5'SS whose usage increases upon *LUC7L2* depletion results in the inclusion of a premature termination codon (PTC) (Figure 5A). Second, skipping of exon 12 deletes 30 amino acids in the catalytic site of the enzyme (Figure S5A). We validated the increased skipping of exon 12 in *LUC7L2*<sup>KO</sup> cells and observed a global decrease in the abundance of the *PFKM* protein (Figure 5B, left). To confirm the effects of this splicing change on *PFKM* levels, we designed an antisense oligonucleotide (ASO) targeting the 5'SS of this exon. Similar to *LUC7L2* depletion, acute ASO treatment led to exon 12 skipping and decreased *PFKM* protein abundance, indicating that the skipping of *PFKM* exon 12 likely yields a less stable protein (Figure 5B, right).

The short time frame of the acute ASO treatment and the potential for long-term toxicity are not compatible with studying slow processes such as glycogen storage, so we opted for cDNA rescue to experimentally address the role of *PFKM* in mediating aspects of the phenotype of *LUC7L2*-depleted cells (Figure S5B). We observed that the overexpression of *PFKM* alone was insufficient to restore the bulk of glycolysis in a *LUC7L2*<sup>KO</sup> background, possibly due to the aforementioned consequences of *LUC7L2* depletion on other glycolytic enzymes. However, it was sufficient to restore normal glycogen storage (Figures 5C and 5D). Our data indicate that *LUC7L2* is required for normal splicing and expression of full-length *PFKM*, and that its absence favors glycogenesis.

### **Expression of *LUC7L2* is limiting for splicing of the cystine/glutamate antiporter *SLC7A11* (xCT)**

Next, we addressed the genetic basis of the second crossover observed in *LUC7L2*-depleted cells at the level of the cystine/glutamate antiporter. Previous studies have shown that this antiporter controls survival in glucose-limiting conditions and

OXPHOS activity (Shin et al., 2017; Koppula et al., 2017). We found that while inhibition with sulfasalazine prevented glutamate secretion and promoted maximal respiration, the overexpression of the *SLC7A11* subunit alone was sufficient to restore glutamate secretion in *LUC7L2*<sup>KO</sup> K562 cells (Figures S5C–S5G), confirming that *SLC7A11* is limiting for glutamate oxidation and OXPHOS. We next examined whether subunits of the system X<sub>c</sub><sup>−</sup> require *LUC7L2* for their expression. *SLC3A2* transcripts were not affected by *LUC7L2* depletion, but we found a significant reduction in the transcript abundance of *SLC7A11* in both *LUC7L2*<sup>KO</sup> HeLa and K562 cells (Figure S5H). Reduced inclusion of *SLC7A11* exon 7 was detected in these cells ( $\Delta\psi = -0.25$ ,  $FDR < 6 \times 10^{-11}$ ), and we noticed that exon 9 also showed reduced inclusion, which was previously annotated and which we confirmed by RT-PCR and Sanger sequencing (Figures 5E, 5F, and S5I). Skipping of exons 7 and/or 9 yield PTCs in *SLC7A11* transcripts, likely reducing mRNA abundance via nonsense-mediated mRNA decay (NMD) (Figure S5J). *LUC7L2* binding was also observed at the 5'SS of these exons by eCLIP (Figure 5E), suggesting a direct effect on their splicing. Accordingly, the depletion of *LUC7L2* led to a decrease in *SLC7A11* expression in K562, HeLa, and HAP1 cells (Figures 5G and S5K). The reduced expression of *SLC7A11* was also observed upon the depletion of *SNRPA* and *SNRNP70*, the 2 other U1 snRNP subunits identified in our screen (Figure S5L), and *LUC7L2* overexpression was sufficient to stabilize *SLC7A11* transcript and protein in K562 cells (Figures S5M and S5N).

To test for a direct contribution of *SLC7A11* splicing to the metabolic phenotypes observed in *LUC7L2*<sup>KO</sup>, we focused on *LUC7L2*<sup>KO</sup> HAP1 cells, a cell line in which the role of this antiporter in antagonizing viability in low glucose conditions is well characterized (Shin et al., 2017). As in K562 cells, we found that *LUC7L2* depletion increased OXPHOS activity (Figure S2F) and viability in galactose (Figure 5H). We then treated WT HAP1 cells with ASOs targeting the 5'SS of *SLC7A11* exons 7 and 9, where *LUC7L2* and the U1 snRNP bind. Similar to the phenotype of *LUC7L2*<sup>KO</sup> cells, we found that acute ASO treatment led to skipping of these exons, preventing *SLC7A11* expression and glutamate secretion, and boosting maximal respiration and viability in galactose (Figures 5I–5L), all resembling the phenotype observed upon *LUC7L2* depletion. We conclude that the splicing of *SLC7A11* (xCT) is sensitive to perturbations of U1 snRNP components, including *LUC7L2*, and that altered splicing of *SLC7A11* induced by *LUC7L2* depletion contributes to the metabolic and viability phenotypes observed in *LUC7L2*<sup>KO</sup> cells (Figures 1 and 3).

### ***LUC7L2* depletion causes secondary accumulation of RC complexes**

To obtain a comprehensive view of proteome remodeling in *LUC7L2*-depleted K562 cells, we next performed global quantitative proteomics (Figures 6A and S6A–S6D). As expected, we observed the depletion of *PFKM* in *LUC7L2*<sup>KO</sup> cells and differential expression of multiple glycolytic enzymes, including rate-determining factors (Tanner et al., 2018) such as hexokinases HK1/2 ( $p < 10^{-2}$ ), the glucose transporter GLUT1 ( $p < 10^{-5}$ ), and the lactate transporter *SLC16A1* ( $p < 0.02$ ) (Table S8).

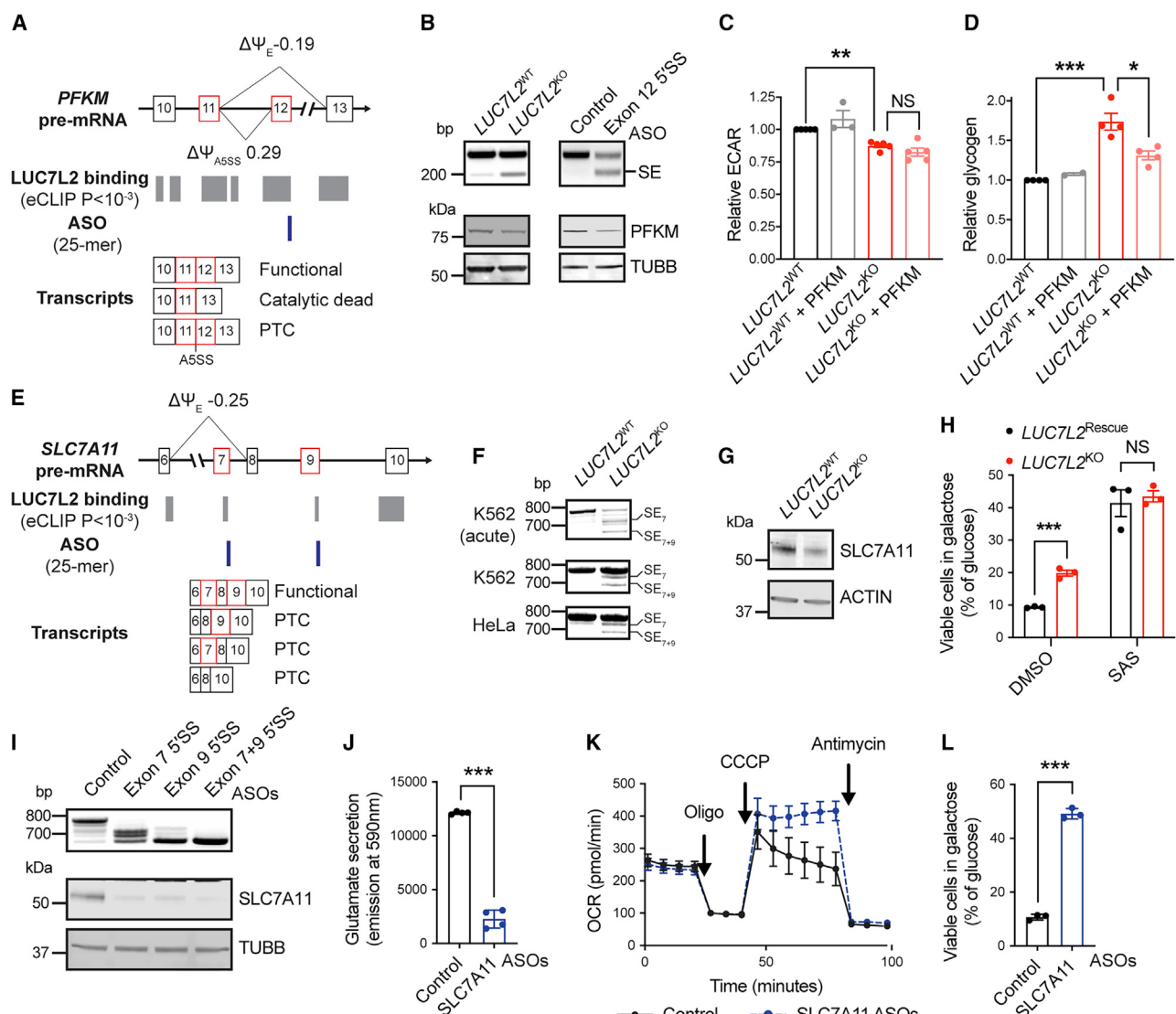


**Figure 5. Role of *LUC7L2*-mediated *PFKM* and *SLC7A11* alternative splicing in energy metabolism**

(A) Representation of *PFKM* exons 10–13, *LUC7L2* binding sites as determined by eCLIP, antisense oligonucleotides (ASO) targeting sites, and the expected transcripts. A negative  $\Delta\Psi$  value indicates exon skipping.  $\Psi$ , percent spliced in reported by rMATs in K562 cells; E, exon; PTC, premature termination codons. (B) RT-PCR (top) and immunoblot (bottom) of *LUC7L2*<sup>KO</sup> K562 cells (left) or HAP1 cells treated for 48 h with ASO targeting the 5'SS of *PFKM* exon 12 (right). (C and D) Relative ECAR (C, n = 3–5) and (D) glycogen in *LUC7L2*<sup>KO</sup> K562 cells expressing control cDNAs (*GFP*) or *PFKM* cDNA (n = 2–4).

(E) Representation of *SLC7A11* exons 6–10 as in (A).

(F) RT-PCR of *LUC7L2*<sup>KO</sup> K562 cells with primers amplifying transcripts corresponding to *SLC7A11* exons 6–12.

(G) Immunoblot on *LUC7L2*<sup>KO</sup> K562 cells with antibodies to *SLC7A11* and ACTIN.

(H) Cell viability of *LUC7L2*<sup>Rescue</sup> (corresponds to *LUC7L2*<sup>KO</sup> expressing *LUC7L2* cDNA) and *LUC7L2*<sup>KO</sup> HAP1 cells grown for 24 h in galactose relative to glucose (n = 3). SAS, 500  $\mu$ M sulfasalazine.

(I) RT-PCR (top) and immunoblot (bottom) of HAP1 cells treated for 48 h with ASOs targeting the 5'SS of exon 7 and/or exon 9 of *SLC7A11*.

(J–L) Media glutamate (J, n = 4), (K) representative Seahorse trace (shown as mean  $\pm$  SD), and (L) viability in the galactose of HAP1 cells treated for 48 h with the indicated ASOs (n = 3).

All data are shown as means  $\pm$  SEMs (unless otherwise stated), with \*p < 0.05, \*\*p < 0.01, and \*\*\*p < 0.001, t test relative to control.

See also Figure S5.

Transcripts of these factors were generally bound by *LUC7L2*, but splicing changes were not always observed in *LUC7L2*<sup>KO</sup> cells, suggesting regulation by both direct and indirect mechanisms. *SLC7A11* was not detected in the proteomics

analysis, possibly owing to its hydrophobicity. Importantly, while abundances of mitochondria and splicing-related proteins were not globally affected, GO analysis revealed a strong enrichment for OXPHOS proteins in *LUC7L2*<sup>KO</sup> cells, with “NADH

# Molecular Cell

## Article

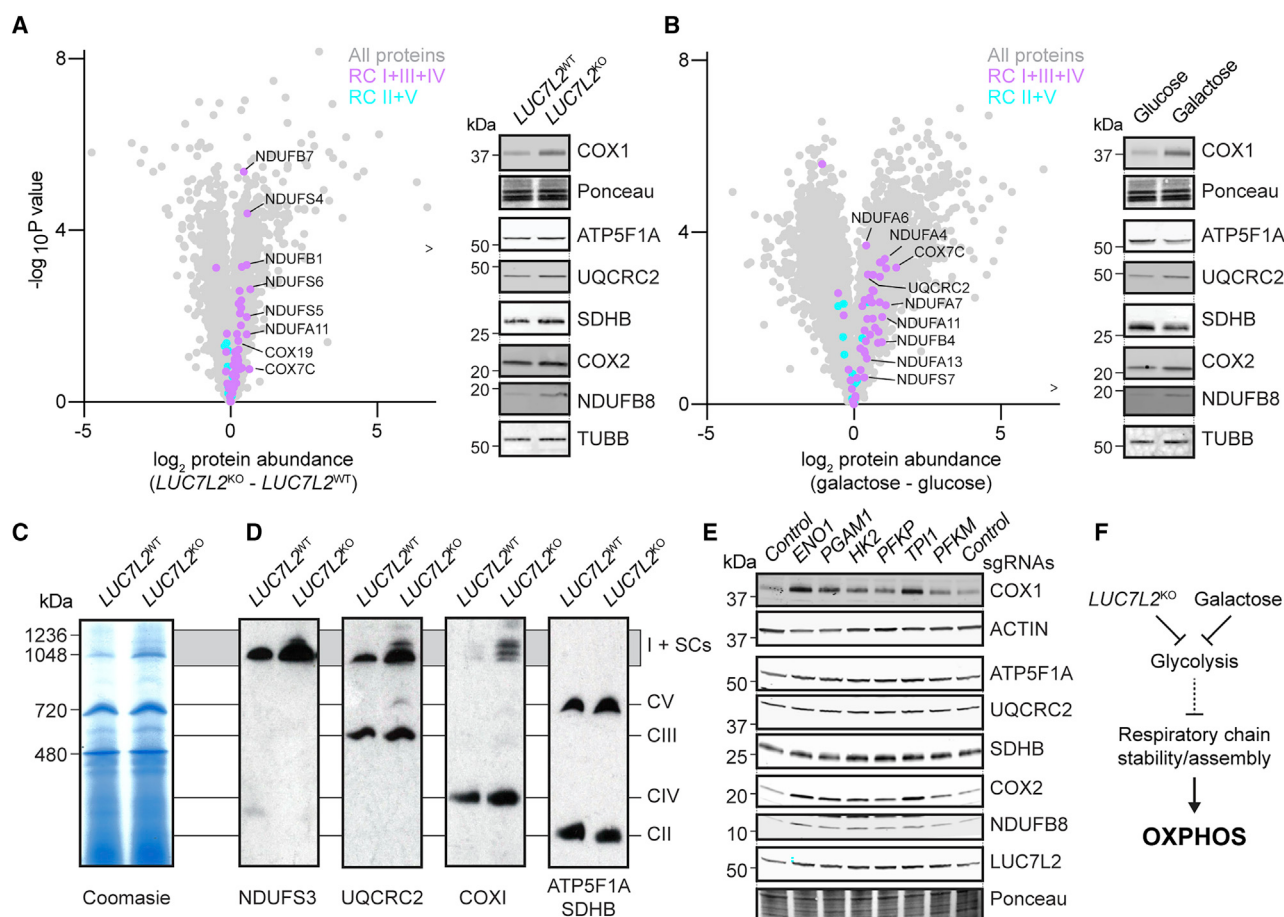


**Figure 6. Proteomic analysis of *LUC7L2*<sup>KO</sup> and galactose-grown cells reveals accumulation of secondary complexes I+III+IV**

(A and B) Volcano plots and immunoblots of OXPHOS protein expression in *LUC7L2*<sup>KO</sup> (A) and (B) in galactose-grown K562 cells. > indicates a protein not shown but reported in Table S8.

(C and D) Blue-native PAGE on a mitochondria-rich fraction isolated from *LUC7L2*<sup>KO</sup> K562 cells and stained with Coomassie (C) or (D) immunoblotted with the indicated antibodies. Parallel blots in which the same lysate was loaded were used to avoid antibodies cross-reactivity. CI-V, complexes I to V; SCs, supercomplexes.

(E) Immunoblot on K562 cells expressing Cas9 and treated with sgRNAs targeting glycolytic enzymes with the indicated antibodies.

(F) Model of the secondary regulation of the respiratory chain by *LUC7L2* and galactose.

See also Figure S6 and Table S8.

dehydrogenase complex” as the top-scoring term associated with upregulated proteins ( $p < 10^{-4}$ ) (Figure S6C).

Given this inverse relationship between abundance of *LUC7L2* and OXPHOS proteins, we analyzed their relative expression in published large-scale proteomics studies. Similar to our experimental observation in cells, *LUC7L2* was significantly anti-correlated with OXPHOS protein expression across organs in 2 *in vivo* mouse tissue proteomic atlases ( $p < 10^{-42}$ , Wilcoxon) (Geiger et al., 2013; Huttlin et al., 2010; Figure S6E). A similar anti-correlation was observed in a proteomics study of brains from healthy subjects or from patients with neurodegenerative disease and showed that *LUC7L2* protein accumulates in patients, whereas OXPHOS proteins are decreased in Parkinson’s disease (Figure S6F; Ping et al., 2018). OXPHOS protein abundance also decreases in skeletal muscle with aging, as recently confirmed by a proteomic study on 58 skeletal muscle biopsies (Ubaida-Mohien

et al., 2019). In this study, too, we observed the significant upregulation of *LUC7L2* with age and anti-correlation with OXPHOS ( $p < 10^{-26}$ , Wilcoxon) (Figure S6E). Thus, in these four *in vivo* datasets, we observed inverse relationships between the abundance of *LUC7L2* and OXPHOS proteins resembling *LUC7L2*<sup>KO</sup> depletion.

OXPHOS proteins also accumulate in glucose-limiting conditions (Rossignol et al., 2004). To compare this condition to *LUC7L2*<sup>KO</sup>, we performed proteomics analysis of galactose-grown cells and observed strong upregulation, as expected (Figure 6B). Importantly, we noticed a similar pattern in both *LUC7L2*<sup>KO</sup> cells and in galactose: the upregulation of subunits of the RC complex I, III, IV. In contrast, protein subunits of RC complex II and the ATP synthase (V), as well as from other mitochondrial protein complexes, and the gene expression machinery were not affected, or rather decreased (Figures 6A, 6B,

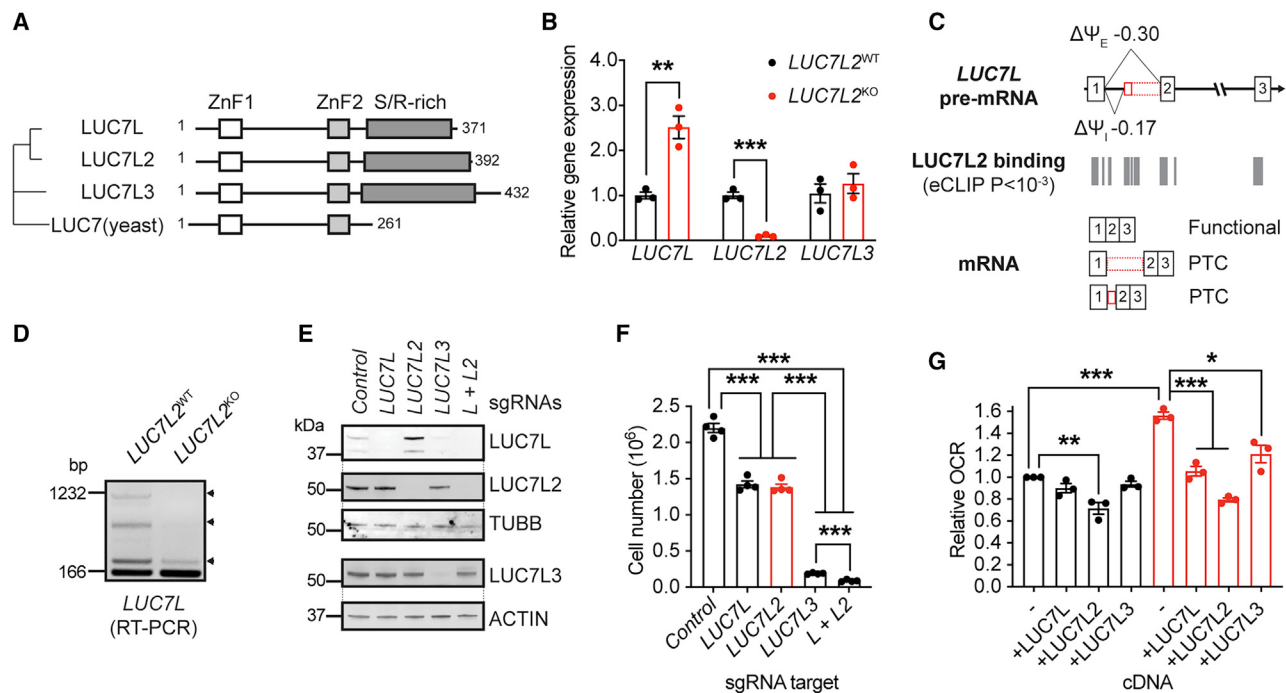


**Figure 7. Pre-mRNA splicing and partial redundancy within the *LUC7* family**

(A) Phylogenetic tree of the LUC7 protein family. LUC7 is from *Saccharomyces cerevisiae*. S/R-rich, serine and arginine-rich domain; ZnF, zinc finger domain.  
 (B) Quantitative PCR detecting *LUC7* family transcripts in *LUC7L2*<sup>KO</sup> K562 cells (n = 3).  
 (C) Representation of *LUC7L* exons 1–3, *LUC7L2* binding sites as determined by eCLIP, and the expected transcripts. I, intron.  
 (D) RT-PCR amplifying *LUC7L* exon 1 to exon 2. Arrowheads: retained entities in *LUC7L*.  
 (E and F) Immunoblot of LUC7 proteins in cell lines expressing Cas9 and sgRNAs targeting the indicated genes using the indicated antibodies (E) and (F) number of cells after 4 days of growth in glucose-containing media.  
 (G) Oxygen consumption analysis of *LUC7L2*<sup>KO</sup> K562 cells expressing cDNAs of *LUC7* family members.  
 All data are shown as means ± SEMs, with \*p < 0.05, \*\*p < 0.01, and \*\*\*p < 0.001, t test relative to control.  
 See also Figure S7.

S6A, S6B, and S6G). Transcripts of RC complexes I+III+IV did not accumulate in *LUC7L2*<sup>KO</sup>, suggesting an effect occurring after RNA processing (Figure S6A). However, the same RC complexes I+III+IV have the ability to interact within the mitochondrial inner membrane to form “supercomplexes” (SCs), and their proposed roles in reinforcing RC complex stability (Acin-Pérez et al., 2004) could explain their accumulation in *LUC7L2*<sup>KO</sup> cells. Accordingly, blue-native PAGE confirmed the accumulation of higher-molecular-weight RC complexes in both K562 and HeLa *LUC7L2*<sup>KO</sup> and galactose-grown cells (Figures 6C, 6D, and S6H).

Galactose growth and *LUC7L2* depletion both attenuate glycolysis, and we next directly tested whether lower glycolytic rates could explain increased RC abundance. We used CRISPR/Cas9 to acutely deplete six glycolytic enzymes and subsequently measured OXPHOS proteins (Figures 6E and S6I). Importantly, we found that the depletion of these genes generally led to the accumulation of the same RC subunits as *LUC7L2*<sup>KO</sup> and galactose, which was particularly apparent upon the depletion of *ENO1* and *TPI1*. While the mechanism by which attenuated glycolysis leads to RC complex accumulation was not investigated here, our observations indicate that the increased abundance of RC complexes in *LUC7L2*<sup>KO</sup> cells is

likely secondary to the effect of this gene on glycolysis (Figure 6F) and possibly involves the stabilization of mitochondrial SCs.

#### Cross-regulation and partial redundancy within the *LUC7* family

Finally, we investigated the role of *LUC7L2* paralogs *LUC7L* and *LUC7L3* in energy metabolism. All three *LUC7* genes encode similar proteins (Tufarelli et al., 2001; Figure 7A). Analysis of LUC7 proteins across a mouse proteomics atlas (Geiger et al., 2013) revealed that although a general anti-correlation with OXPHOS was observed for all 3 proteins, the expression patterns of individual members of the LUC7 family were not identical (Figure S7). For example, *LUC7L* was present at higher levels in the brain, while expression of *LUC7L3* was not detectable in the spleen, suggesting tissue-specific roles in splicing.

With 85% protein identity, *LUC7L* is the closest homolog to *LUC7L2*. This gene was also one of the most affected genes in *LUC7L2*<sup>KO</sup> (Figure 7B), and we found decreased inclusion of an annotated exon located in an intron between canonical exons 1 and 2 of *LUC7L*, as well as decreased retention of the associated intron, all within a region highly bound by *LUC7L2* ( $\Delta\Psi_E = -0.30$  and  $\Delta\Psi_I = -0.17$ , respectively) (Figures 7C and 7D). Importantly, inclusion of the exon with or without intron retention results in a

# Molecular Cell

## Article



PTC in *LUC7L*, which likely leads to transcript degradation by NMD. Accordingly, protein analysis revealed strong upregulation of *LUC7L* in *LUC7L2<sup>KO</sup>* cells, indicating a repressive role for *LUC7L2* (Figure 7E; Table S8), an observation that is relatively common among paralogous RNA-binding proteins (Spellman et al., 2007; Ni et al., 2007; Lareau et al., 2007).

To experimentally address the function of each of the *LUC7* genes, we depleted each individually, as well as *LUC7L* and *LUC7L2* together (Figure 7E). We found that the depletion of *LUC7L* or *LUC7L2* individually led to a mild defect in cell proliferation (Figure 7F), while the depletion of *LUC7L3* caused a strong growth defect. Simultaneous depletion of *LUC7L* and *LUC7L2* showed a synthetic lethal phenotype, consistent with some degree of functional redundancy and cross-regulation. To directly address redundancy, we investigated whether members of the *LUC7* family could rescue the metabolic phenotype observed in *LUC7L2<sup>KO</sup>* cells. For this purpose, we stably expressed *LUC7L*, *LUC7L2*, or *LUC7L3* in these cells and measured oxygen consumption. Importantly, we found that while the expression of *LUC7L2* alone was able to decrease OCR in WT cells (Figure 7G), re-expression of any of the members of the family could restore normal oxygen consumption in *LUC7L2<sup>KO</sup>* cells to varying degrees (Figure 7G). Our observations implicate all of the members of the *LUC7* family in energy metabolism.

## DISCUSSION

We have found that the expression of genes related to pre-mRNA splicing and the U1 snRNP affect the balance between glycolysis and OXPHOS. Genetic loss of any of 3 U1 snRNP-specific subunits (SNRPA, SNRNP70, *LUC7L2*) boosts cellular fitness when glycolysis is compromised. The U1 snRNP plays an essential role in pre-mRNA splicing and modulates other nuclear RNA-related processes such as cleavage and polyadenylation (Berg et al., 2012) and chromatin retention of non-coding RNAs (Yin et al., 2020). To our knowledge, our work is the first to establish a link between the expression of U1 snRNP components and the bioenergetic state of the cell.

In the present study, we were able to confirm that *LUC7L2* is a genuine component of the U1 snRNP in humans, as has been observed for *LUC7* homologs in yeast and plants (de Francisco Amorim et al., 2018; Fortes et al., 1999). Padgett and colleagues have independently reached this same conclusion in an accompanying paper (Daniels et al., 2021). Because *LUC7* genes are expressed in a tissue-specific manner (Figure S7), as are some of the transcripts of metabolic genes bound by *LUC7L2*, we speculate that the relative abundance of these paralogs in different cells may contribute to differences in levels of OXPHOS and glycolysis between different cell types.

We show that the loss of *LUC7L2* results in an activation of OXPHOS. The full set of mechanisms linking *LUC7L2* expression of energy metabolism are likely complex, involving both direct and indirect mechanisms. Given that the U1 snRNP plays central roles in splicing and gene expression, we searched for changes in our transcriptome analysis that may help explain the observed metabolic phenotype. In the present study, we have prioritized observations from our metabolic characterization of *LUC7L2<sup>KO</sup>* cells (Figures 1, 2, and 3) and investigated in detail *PFKM* and

*SLC7A11*, which we show contribute to key aspects of the metabolic phenotype following the depletion of *LUC7L2* (Figure 5).

First, we found that *LUC7L2* binds to and contributes to splicing and expression of *PFKM* (Figure 5A). This enzyme alone did not explain the global decrease in glycolysis in *LUC7L2<sup>KO</sup>* cells, as we found multiple instances of altered expression in glycolytic proteins in *LUC7L2<sup>KO</sup>* (Table S8), including in rate-limiting factors (Tanner et al., 2018). We propose that these changes may collectively lead to the decreased glycolytic activity in *LUC7L2<sup>KO</sup>* cells, and likely originate from both primary and secondary mechanisms. However, we show that altered splicing in *PFKM* is likely directly responsible for the glycogen storage phenotype in *LUC7L2<sup>KO</sup>* cells. The differential role of *PFKM* in glycogen storage versus glycolysis is not unexpected from observations of patients with Tarui disease, who present minimal effects on circulating lactate at rest (Piirilä et al., 2016), possibly due to the complex interplay between *PFKM*, its paralogs, and allosterity.

Second, we have identified alternative splicing events in *SLC7A11* whereby skipping of exons 7 and 9 leads to the loss of *SLC7A11* (xCT) protein, which has a direct impact on OXPHOS. xCT has emerged as a critical regulator of metabolism and cell viability, and while high expression of this cystine/glutamate antiporter blunts glutamine anaplerosis and creates a dependency on glycolysis for ATP production (Koppula et al., 2017; Shin et al., 2017), genetic ablation of this cancer-related gene in tumors induces death by lipid peroxidation (Badgley et al., 2020). Expression of *SLC7A11* is highly regulated and is known to be transcriptionally activated by ATF4 (Sato et al., 2004) and NRF2 (Shin et al., 2017) and repressed by P53 (Jiang et al., 2015). *SLC7A11* activity is also regulated by direct mammalian target of rapamycin complex 2 (mTORC2) phosphorylation (Gu et al., 2017). Our work adds another layer of complexity to the regulation of this transporter. In the future, it will be interesting to determine whether these splicing events are regulated in disease states to influence the sensitivity to lipid peroxidation.

In addition, we report that, in general, shifts from glycolysis to OXPHOS appear to be associated with an accumulation of RC complexes (Figure 6). When cells are grown in galactose or in glucose-grown cells following genetic ablation of *LUC7L2* or of glycolytic enzymes, we observed a characteristic pattern of RC I+III+IV accumulation, which prompted us to investigate the assembly of the SCs. Future studies are needed to determine how the reduction in glycolysis affects RC assembly.

Our work predicts that a shift in energy metabolism will accompany human conditions associated with mis-expression of *LUC7L2* and the U1 snRNP. U1 dysregulation and mutations have been reported to occur in cancer (Shuai et al., 2019; Suzuki et al., 2019; Oh et al., 2020). Similarly, mutations in *LUC7L2* or haploinsufficiency through the loss of chromosome 7q are associated with MDS (Singh et al., 2013). 7q- models recapitulate differentiation defects observed in MDS (Kotini et al., 2015), and the reintroduction of *LUC7L2* is sufficient to restore differentiation. How *LUC7L2* loss affects hematopoietic stem cell differentiation and MDS is not clear, but our work raises the possibility of a bioenergetics-related mechanism. It is notable that other splicing factors associated with MDS also participate in the splicing of

metabolic enzymes; for example, MDS-associated mutations in *SRSF2* give rise to the same splicing change in *PFKM* (Zhang et al., 2015) as we observe in *LUC7L2*<sup>KO</sup>. Our work has revealed a novel metabolic vulnerability of *LUC7L2*-depleted cells (Figure 2C) and predicts that pharmacological blockade of OXPHOS using drugs such as metformin may be beneficial in these disorders.

While the present analysis has focused on the effects of *LUC7L2* gene depletion, an exciting future direction is to determine whether metabolism is regulated by changes in the expression of *LUC7* family members in normal development or physiology. We observe a consistent, inverse correlation between the protein levels of *LUC7L2* and OXPHOS across organs and during disease and aging (Figure S6). Expression of *LUC7L2* and its paralogs is known to respond to changes in the environment, including changes in oxygen tension (Kimura et al., 2004; Gao et al., 2011). It is notable that previous proteomics studies have established that *LUC7L2* is post-translationally modified via phosphorylation and hydroxylation (Webby et al., 2009; Dephoure et al., 2008). In this context, it is possible that proteins of the *LUC7* family, as well as other U1 snRNP components, may integrate signals such as oxygen and nutrients to balance the activity of major pathways in energy metabolism.

### Limitations of study

Pre-mRNA splicing, gene expression and energy metabolism are cell type-specific processes. We report here that *LUC7L2* loss affects energy metabolism in three cellular models, but there are differences across cell types. For example, while we observed decreased levels of *SLC7A11* in 3 *LUC7L2*<sup>KO</sup> cell lines investigated (Figures 5G and S5K), it led to an increase in net oxygen consumption only in K562 and HAP1 cells, but not in HeLa cells (Figure S2E). It is possible that cells with different metabolic programs, for instance, based on low *SLC7A11* and *PFKM* expression or cells with high expression of *LUC7L* and *LUC7L3* may be indifferent to *LUC7L2* depletion. Furthermore, although we observed that *LUC7L2* depletion results in altered splicing in *PFKM*, *SLC7A11*, and other genes, and that *LUC7L2* cross-links near the regulated exons in *PFKM* and *SLC7A11*, this does not formally prove that the effect on splicing is direct. Our profiling experiments of *LUC7L2*<sup>KO</sup> cells were likely biased toward abundant molecules, including in our sequencing analysis, as well as for the detection of peptides and metabolites by MS. Thus, it is possible that additional low-abundance splicing events in *LUC7L2*<sup>KO</sup> cells may have been missed and that those events may affect additional metabolic aspects in *LUC7L2*-depleted cells.

### STAR★METHODS

Detailed methods are provided in the online version of this paper and include the following:

- KEY RESOURCES TABLE
- RESOURCE AVAILABILITY
  - Lead contact
  - Materials availability
  - Data and code availability

### ● EXPERIMENTAL MODEL AND SUBJECT DETAILS

- Cell lines
- METHOD DETAILS
  - CRISPR screen re-analysis
  - Cell culture and cell growth assays
  - Gene-specific CRISPR-Cas9 knockouts
  - Antisense oligonucleotides (ASOs) treatment
  - Oxygen consumption and extracellular acidification rates by Seahorse XF analyzer
  - Media acidification
  - Mitochondrial and nuclear DNA determination
  - RNA extraction, reverse transcription, and qPCR
  - Citrate synthase activity determination
  - Glycogen determinationS
  - Glutamate determination
  - Cell viability assay in galactose
  - Electron microscopy
  - Confocal microscopy and immunofluorescence
  - Polyacrylamide gel electrophoresis and immunoblotting
  - Liquid chromatography-mass spectrometry (LC-MS)
  - *LUC7L2*-3xFLAG immunoprecipitation and mass spectrometry
  - Enhanced crosslinking and immunoprecipitation (eCLIP)
  - Blue-native PAGE
  - Mitochondrial translation
  - Gene-specific cDNA cloning and expression
  - Quantitative proteomics
  - Next-generation RNA sequencing

### ● QUANTIFICATION AND STATISTICAL ANALYSIS

- eCLIP
- Gene expression
- Splicing
- Overlap
- Correlation
- Gene Ontology

### SUPPLEMENTAL INFORMATION

Supplemental information can be found online at <https://doi.org/10.1016/j.molcel.2021.02.033>.

### ACKNOWLEDGMENTS

We thank J. Wengrod, T.L. To, and the V.K.M. laboratory for advice and feedback on the manuscript; M. Shadpour for technical help; and D. Steensma, B. Ebert, M. Blower, A. Kotini, and E. Papapetrou for fruitful discussion. This work was supported by NIH grants R35GM122455 (to V.K.M.), R01GM085319 (to C.B.B.), HG004659, and U41HG009889 (to G.W.Y.), EMBO long-term ALTF 554-2015 and a SNF Advanced Postdoc.Mobility P300PA\_171514 fellowship (to A.A.J.), and a F32 Fellowship from the National Institute of General Medical Sciences 1F32GM133047-01 (to O.S.S.). V.K.M. is an Investigator of the Howard Hughes Medical Institute.

### AUTHOR CONTRIBUTIONS

A.A.J. worked under the supervision of V.K.M. to design, perform, and analyze all of the experiments, with the exception of the gene expression data analysis (E.M. and B.E.B.), eCLIP (S.M.B. and G.W.Y. supervision), eCLIP and splicing data analysis (B.E.B. and C.B.B. supervision), metabolite profiling (H.S.,

# Molecular Cell

## Article



O.S.S., and R.S.), and correlation analysis (S.E.C.). A.A.J. and V.K.M. wrote the manuscript with input from all of the authors.

### DECLARATION OF INTERESTS

V.K.M. is a paid scientific advisor to 5AM Ventures and Janssen Pharmaceuticals. O.S.S. is a paid consultant for Proteinaceous. R.S. holds equity in Blue-Bird Bio. G.W.Y. is co-founder, member of the Board of Directors, on the scientific advisory board, equity holder, and paid consultant for Locanabio and Eclipse BioInnovations. G.W.Y. is a visiting professor at the National University of Singapore. G.W.Y.'s interest(s) have been reviewed and approved by the University of California, San Diego in accordance with its conflict of interest policies. A.A.J. and V.K.M. are co-inventors on a US provisional patent application related to the work in this manuscript. The authors declare no other competing interests.

### INCLUSION AND DIVERSITY

One or more of the authors of this paper self-identifies as a member of the LGBTQ+ community. The author list of this paper includes contributors from the location where the research was conducted who participated in the data collection, design, analysis, and/or interpretation of the work.

Received: June 21, 2020

Revised: December 18, 2020

Accepted: February 22, 2021

Published: April 13, 2021

### REFERENCES

- Acín-Pérez, R., Bayona-Bafaluy, M.P., Fernández-Silva, P., Moreno-Loshuertos, R., Pérez-Martos, A., Bruno, C., Moraes, C.T., and Enríquez, J.A. (2004). Respiratory complex III is required to maintain complex I in mammalian mitochondria. *Mol. Cell* 13, 805–815.
- Arroyo, J.D., Jourdain, A.A., Calvo, S.E., Ballarano, C.A., Doench, J.G., Root, D.E., and Mootha, V.K. (2016). A Genome-wide CRISPR Death Screen Identifies Genes Essential for Oxidative Phosphorylation. *Cell Metab.* 24, 875–885.
- Badgley, M.A., Kremer, D.M., Maurer, H.C., DelGiorno, K.E., Lee, H.J., Purohit, V., Sagalovskiy, I.R., Ma, A., Kapilian, J., Firl, C.E.M., et al. (2020). Cysteine depletion induces pancreatic tumor ferroptosis in mice. *Science* 368, 85–89.
- Bao, X.R., Ong, S.E., Goldberger, O., Peng, J., Sharma, R., Thompson, D.A., Vafai, S.B., Cox, A.G., Marutani, E., Ichinose, F., et al. (2016). Mitochondrial dysfunction remodels one-carbon metabolism in human cells. *eLife* 5, e10575.
- Berg, M.G., Singh, L.N., Younis, I., Liu, Q., Pinto, A.M., Kaida, D., Zhang, Z., Cho, S., Sherrill-Mix, S., Wan, L., and Dreyfuss, G. (2012). U1 snRNP determines mRNA length and regulates isoform expression. *Cell* 150, 53–64.
- Bonnet, S., Archer, S.L., Allalunis-Turner, J., Haromy, A., Beaulieu, C., Thompson, R., Lee, C.T., Lopaschuk, G.D., Puttagunta, L., Bonnet, S., et al. (2007). A mitochondria-K<sup>+</sup> channel axis is suppressed in cancer and its normalization promotes apoptosis and inhibits cancer growth. *Cancer Cell* 11, 37–51.
- Bray, N.L., Pimentel, H., Melsted, P., and Pachter, L. (2016). Near-optimal probabilistic RNA-seq quantification. *Nat. Biotechnol.* 34, 525–527.
- Christofk, H.R., Vander Heiden, M.G., Harris, M.H., Ramanathan, A., Gerszten, R.E., Wei, R., Fleming, M.D., Schreiber, S.L., and Cantley, L.C. (2008). The M2 splice isoform of pyruvate kinase is important for cancer metabolism and tumour growth. *Nature* 452, 230–233.
- Crabtree, H.G. (1929). Observations on the carbohydrate metabolism of tumours. *Biochem. J.* 23, 536–545.
- Daniels, N.J., Hershberger, C.E., Gu, X., Schueger, C., DiPasquale, W.M., Brick, J., Sauntharajah, Y., Maciejewski, J.P., and Padgett, R.A. (2021). Functional analyses of human LUC7-like proteins involved in splicing regulation and myeloid neoplasms. *Cell Rep* 35, 108989.
- De Conti, L., Baralle, M., and Buratti, E. (2013). Exon and intron definition in pre-mRNA splicing. *Wiley Interdiscip. Rev. RNA* 4, 49–60.
- de Francisco Amorim, M., Willing, E.M., Szabo, E.X., Francisco-Manglet, A.G., Droste-Borel, I., Maćek, B., Schneeberger, K., and Laubinger, S. (2018). The U1 snRNP Subunit LUC7 Modulates Plant Development and Stress Responses via Regulation of Alternative Splicing. *Plant Cell* 30, 2838–2854.
- Dephoure, N., Zhou, C., Villén, J., Beausoleil, S.A., Bakalarski, C.E., Elledge, S.J., and Gygi, S.P. (2008). A quantitative atlas of mitotic phosphorylation. *Proc. Natl. Acad. Sci. USA* 105, 10762–10767.
- Dobin, A., Davis, C.A., Schlesinger, F., Drenkow, J., Zaleski, C., Jha, S., Batut, P., Chaisson, M., and Gingeras, T.R. (2013). STAR: ultrafast universal RNA-seq aligner. *Bioinformatics* 29, 15–21.
- Eden, E., Navon, R., Steinfield, I., Lipson, D., and Yakhini, Z. (2009). GOrilla: a tool for discovery and visualization of enriched GO terms in ranked gene lists. *BMC Bioinformatics* 10, 48.
- Fortes, P., Bilbao-Cortés, D., Fornerod, M., Rigaut, G., Raymond, W., Séraphin, B., and Mattaj, I.W. (1999). Luc7p, a novel yeast U1 snRNP protein with a role in 5' splice site recognition. *Genes Dev.* 13, 2425–2438.
- Friedman, B.A., Stadler, M.B., Shomron, N., Ding, Y., and Burge, C.B. (2008). Ab initio identification of functionally interacting pairs of cis-regulatory elements. *Genome Res.* 18, 1643–1651.
- Gao, G., Xie, A., Huang, S.C., Zhou, A., Zhang, J., Herman, A.M., Ghassemzadeh, S., Jeong, E.M., Kasturirangan, S., Raicu, M., et al. (2011). Role of RBM25/LUC7L3 in abnormal cardiac sodium channel splicing regulation in human heart failure. *Circulation* 124, 1124–1131.
- Gao, J., Schatton, D., Martinelli, P., Hansen, H., Pla-Martin, D., Barth, E., Becker, C., Altmüller, J., Frommolt, P., Sardiello, M., and Rugarli, E.I. (2014). CLUH regulates mitochondrial biogenesis by binding mRNAs of nuclear-encoded mitochondrial proteins. *J. Cell Biol.* 207, 213–223.
- Geiger, T., Velic, A., Macek, B., Lundberg, E., Kampf, C., Nagaraj, N., Uhlen, M., Cox, J., and Mann, M. (2013). Initial quantitative proteomic map of 28 mouse tissues using the SILAC mouse. *Mol. Cell. Proteomics* 12, 1709–1722.
- Gohil, V.M., Sheth, S.A., Nilsson, R., Wojtovich, A.P., Lee, J.H., Perocchi, F., Chen, W., Clish, C.B., Ayata, C., Brookes, P.S., and Mootha, V.K. (2010). Nutrient-sensitized screening for drugs that shift energy metabolism from mitochondrial respiration to glycolysis. *Nat. Biotechnol.* 28, 249–255.
- Gu, Y., Albuquerque, C.P., Braas, D., Zhang, W., Villa, G.R., Bi, J., Ikegami, S., Masui, K., Gini, B., Yang, H., et al. (2017). mTORC2 Regulates Amino Acid Metabolism in Cancer by Phosphorylation of the Cystine-Glutamate Antiporter xCT. *Mol. Cell* 67, 128–138.e7.
- Hayer, A., Shao, L., Chung, M., Joubert, L.M., Yang, H.W., Tsai, F.C., Bisaria, A., Betzig, E., and Meyer, T. (2016). Engulfed cadherin fingers are polarized junctional structures between collectively migrating endothelial cells. *Nat. Cell Biol.* 18, 1311–1323.
- Hillenmeyer, M.E., Fung, E., Wildenhain, J., Pierce, S.E., Hoon, S., Lee, W., Proctor, M., St Onge, R.P., Tyers, M., Koller, D., et al. (2008). The chemical genomic portrait of yeast: uncovering a phenotype for all genes. *Science* 320, 362–365.
- Huang, L.E., Gu, J., Schau, M., and Bunn, H.F. (1998). Regulation of hypoxia-inducible factor 1alpha is mediated by an O2-dependent degradation domain via the ubiquitin-proteasome pathway. *Proc. Natl. Acad. Sci. USA* 95, 7987–7992.
- Hutlin, E.L., Jedrychowski, M.P., Elias, J.E., Goswami, T., Rad, R., Beausoleil, S.A., Villén, J., Haas, W., Sowa, M.E., and Gygi, S.P. (2010). A tissue-specific atlas of mouse protein phosphorylation and expression. *Cell* 143, 1174–1189.
- Ito, K., and Suda, T. (2014). Metabolic requirements for the maintenance of self-renewing stem cells. *Nat. Rev. Mol. Cell Biol.* 15, 243–256.
- Jiang, L., Kon, N., Li, T., Wang, S.J., Su, T., Hibshoosh, H., Baer, R., and Gu, W. (2015). Ferroptosis as a p53-mediated activity during tumour suppression. *Nature* 520, 57–62.
- Jourdain, A.A., Koppen, M., Wydro, M., Rodley, C.D., Lightowers, R.N., Chrzanowska-Lightowers, Z.M., and Martinou, J.C. (2013). GRSF1 regulates RNA processing in mitochondrial RNA granules. *Cell Metab.* 17, 399–410.

- Kimura, E., Hidaka, K., Kida, Y., Morisaki, H., Shirai, M., Araki, K., Suzuki, M., Yamamura, K.I., and Morisaki, T. (2004). Serine-arginine-rich nuclear protein Luc7l regulates myogenesis in mice. *Gene* 341, 41–47.
- Koppula, P., Zhang, Y., Shi, J., Li, W., and Gan, B. (2017). The glutamate/cysteine antiporter SLC7A11/xCT enhances cancer cell dependency on glucose by exporting glutamate. *J. Biol. Chem.* 292, 14240–14249.
- Kotini, A.G., Chang, C.J., Boussaad, I., Delrow, J.J., Dolezal, E.K., Nagulapally, A.B., Perna, F., Fishbein, G.A., Klimek, V.M., Hawkins, R.D., et al. (2015). Functional analysis of a chromosomal deletion associated with myelodysplastic syndromes using isogenic human induced pluripotent stem cells. *Nat. Biotechnol.* 33, 646–655.
- Lareau, L.F., Inada, M., Green, R.E., Wengrod, J.C., and Brenner, S.E. (2007). Unproductive splicing of SR genes associated with highly conserved and ultra-conserved DNA elements. *Nature* 446, 926–929.
- Li, W., Xu, H., Xiao, T., Cong, L., Love, M.I., Zhang, F., Irizarry, R.A., Liu, J.S., Brown, M., and Liu, X.S. (2014). MAGeCK enables robust identification of essential genes from genome-scale CRISPR/Cas9 knockout screens. *Genome Biol.* 15, 554.
- Li, X., Liu, S., Jiang, J., Zhang, L., Espinosa, S., Hill, R.C., Hansen, K.C., Zhou, Z.H., and Zhao, R. (2017). CryoEM structure of *Saccharomyces cerevisiae* U1 snRNP offers insight into alternative splicing. *Nat. Commun.* 8, 1035.
- Lovci, M.T., Ghanem, D., Marr, H., Arnold, J., Gee, S., Parra, M., Liang, T.Y., Stark, T.J., Gehman, L.T., Hoon, S., et al. (2013). Rbfox proteins regulate alternative mRNA splicing through evolutionarily conserved RNA bridges. *Nat. Struct. Mol. Biol.* 20, 1434–1442.
- Love, M.I., Huber, W., and Anders, S. (2014). Moderated estimation of fold change and dispersion for RNA-seq data with DESeq2. *Genome Biol.* 15, 550.
- Ni, J.Z., Grate, L., Donohue, J.P., Preston, C., Nobida, N., O'Brien, G., Shiu, L., Clark, T.A., Blume, J.E., and Ares, M., Jr. (2007). Ultraconserved elements are associated with homeostatic control of splicing regulators by alternative splicing and nonsense-mediated decay. *Genes Dev.* 21, 708–718.
- Oh, J.M., Venters, C.C., Di, C., Pinto, A.M., Wan, L., Younis, I., Cai, Z., Arai, C., So, B.R., Duan, J., and Dreyfuss, G. (2020). U1 snRNP regulates cancer cell migration and invasion in vitro. *Nat. Commun.* 11, 1.
- Pasteur, L. (1861). Animalcules infusoires vivant sans gaz oxygène libre et déterminant des fermentations. *C. R. Acad. Sci.* 52, 344–347.
- Pearce, E.L., Poffenberger, M.C., Chang, C.H., and Jones, R.G. (2013). Fueling immunity: insights into metabolism and lymphocyte function. *Science* 342, 1242454.
- Perez-Riverol, Y., Csordas, A., Bai, J., Bernal-Llinares, M., Hewapathirana, S., Kundu, D.J., Inuganti, A., Griss, J., Mayer, G., Eisenacher, M., et al. (2019). The PRIDE database and related tools and resources in 2019: improving support for quantification data. *Nucleic Acids Res.* 47 (D1), D442–D450.
- Pfeiffer, T., Schuster, S., and Bonhoeffer, S. (2001). Cooperation and competition in the evolution of ATP-producing pathways. *Science* 292, 504–507.
- Piirilä, P., Similä, M.E., Palmio, J., Wuorimaa, T., Ylikallio, E., Sandell, S., Haapalahti, P., Uotila, L., Tyynismaa, H., Udd, B., and Auranen, M. (2016). Unique Exercise Lactate Profile in Muscle Phosphofructokinase Deficiency (Taruji Disease); Difference Compared with McArdle Disease. *Front. Neurol.* 7, 82.
- Ping, L., Duong, D.M., Yin, L., Gearing, M., Lah, J.J., Levey, A.I., and Seyfried, N.T. (2018). Global quantitative analysis of the human brain proteome in Alzheimer's and Parkinson's Disease. *Sci. Data* 5, 180036.
- Plaschka, C., Lin, P.C., Charenton, C., and Nagai, K. (2018). Prespliceosome structure provides insights into spliceosome assembly and regulation. *Nature* 559, 419–422.
- Puigserver, P., Wu, Z., Park, C.W., Graves, R., Wright, M., and Spiegelman, B.M. (1998). A cold-inducible coactivator of nuclear receptors linked to adaptive thermogenesis. *Cell* 92, 829–839.
- Reitzer, L.J., Wice, B.M., and Kennell, D. (1979). Evidence that glutamine, not sugar, is the major energy source for cultured HeLa cells. *J. Biol. Chem.* 254, 2669–2676.
- Rino, J., Carvalho, T., Braga, J., Desterro, J.M., Lührmann, R., and Carmo-Fonseca, M. (2007). A stochastic view of spliceosome assembly and recycling in the nucleus. *PLoS Comput. Biol.* 3, 2019–2031.
- Robinson, B.H., Petrova-Benedict, R., Buncic, J.R., and Wallace, D.C. (1992). Nonviability of cells with oxidative defects in galactose medium: a screening test for affected patient fibroblasts. *Biochem. Med. Metab. Biol.* 48, 122–126.
- Rossignol, R., Gilkerson, R., Aggeler, R., Yamagata, K., Remington, S.J., and Capaldi, R.A. (2004). Energy substrate modulates mitochondrial structure and oxidative capacity in cancer cells. *Cancer Res.* 64, 985–993.
- Sato, H., Tamba, M., Ishii, T., and Bannai, S. (1999). Cloning and expression of a plasma membrane cystine/glutamate exchange transporter composed of two distinct proteins. *J. Biol. Chem.* 274, 11455–11458.
- Sanjana, N.E., Shalem, O., and Zhang, F. (2014). Improved vectors and genome-wide libraries for CRISPR screening. *Nat Methods* 11, 783–784, <https://doi.org/10.1038/nmeth.3047>.
- Sato, H., Nomura, S., Maebara, K., Sato, K., Tamba, M., and Bannai, S. (2004). Transcriptional control of cystine/glutamate transporter gene by amino acid deprivation. *Biochem. Biophys. Res. Commun.* 325, 109–116.
- Shen, S., Park, J.W., Lu, Z.X., Lin, L., Henry, M.D., Wu, Y.N., Zhou, Q., and Xing, Y. (2014). rMATS: robust and flexible detection of differential alternative splicing from replicate RNA-Seq data. *Proc. Natl. Acad. Sci. USA* 111, E5593–E5601.
- Shin, C.S., Mishra, P., Watrous, J.D., Carelli, V., D'Aurelio, M., Jain, M., and Chan, D.C. (2017). The glutamate/cysteine xCT antiporter antagonizes glutamine metabolism and reduces nutrient flexibility. *Nat. Commun.* 8, 15074.
- Shuai, S., Suzuki, H., Diaz-Navarro, A., Nadeu, F., Kumar, S.A., Gutierrez-Fernandez, A., Delgado, J., Pinyol, M., López-Otín, C., Puente, X.S., et al. (2019). The U1 spliceosomal RNA is recurrently mutated in multiple cancers. *Nature* 574, 712–716.
- Singh, H., Lane, A.A., Correll, M., Przychodzen, B., Sykes, D.B., Stone, R.M., Ballen, K.K., Amrein, P.C., Maciejewski, J., and Attar, E.C. (2013). Putative RNA-splicing gene LUC7L2 on 7q34 represents a candidate gene in pathogenesis of myeloid malignancies. *Blood Cancer J* 3, e117, <https://doi.org/10.1038/bcj.2013.16>.
- Spellman, R., Llorian, M., and Smith, C.W. (2007). Crossregulation and functional redundancy between the splicing regulator PTB and its paralogs nPTB and ROD1. *Mol. Cell* 27, 420–434.
- Suzuki, H., Kumar, S.A., Shuai, S., Diaz-Navarro, A., Gutierrez-Fernandez, A., De Antonellis, P., Cavalli, F.M.G., Jurascak, K., Farooq, H., Shibahara, I., et al. (2019). Recurrent non-coding U1-snRNA mutations drive cryptic splicing in Shh medulloblastoma. *Nature* 574, 707–711.
- Tanner, L.B., Goglia, A.G., Wei, M.H., Sehgal, T., Parsons, L.R., Park, J.O., White, E., Toettcher, J.E., and Rabinowitz, J.D. (2018). Four Key Steps Control Glycolytic Flux in Mammalian Cells. *Cell Syst.* 7, 49–62.e8.
- Tarui, S., Okuno, G., Ikura, Y., Tanaka, T., Suda, M., and Nishikawa, M. (1965). Phosphofructokinase Deficiency in Skeletal Muscle. A New Type of Glycogenosis. *Biochem. Biophys. Res. Commun.* 19, 517–523.
- To, T.L., Cuadros, A.M., Shah, H., Hung, W.H.W., Li, Y., Kim, S.H., Rubin, D.H.F., Boe, R.H., Rath, S., Eaton, J.K., et al. (2019). A Compendium of Genetic Modifiers of Mitochondrial Dysfunction Reveals Intra-organelle Buffering. *Cell* 179, 1222–1238.e17.
- Tufarelli, C., Frischauft, A.M., Hardison, R., Flint, J., and Higgs, D.R. (2001). Characterization of a widely expressed gene (LUC7-LIKE; LUC7L) defining the centromeric boundary of the human alpha-globin domain. *Genomics* 71, 307–314.
- Ubaida-Mohien, C., Lyashkov, A., Gonzalez-Freire, M., Tharakan, R., Shardell, M., Moaddel, R., Semba, R.D., Chia, C.W., Gorospe, M., Sen, R., and Ferrucci, L. (2019). Discovery proteomics in aging human skeletal muscle finds change in spliceosome, immunity, proteostasis and mitochondria. *eLife* 8, e49874.
- Van Nostrand, E.L., Pratt, G.A., Shishkin, A.A., Gelboin-Burkhart, C., Fang, M.Y., Sundararaman, B., Blue, S.M., Nguyen, T.B., Surka, C., Elkins, K., et al. (2016). Robust transcriptome-wide discovery of RNA-binding protein binding sites with enhanced CLIP (eCLIP). *Nat. Methods* 13, 508–514.

# Molecular Cell

## Article



- Van Nostrand, E.L., Nguyen, T.B., Gelboin-Burkhart, C., Wang, R., Blue, S.M., Pratt, G.A., Louie, A.L., and Yeo, G.W. (2017). Robust, Cost-Effective Profiling of RNA Binding Protein Targets with Single-end Enhanced Crosslinking and Immunoprecipitation (seCLIP). *Methods Mol. Biol.* **1648**, 177–200.
- Van Nostrand, E.L., Freese, P., Pratt, G.A., Wang, X., Wei, X., Xiao, R., Blue, S.M., Chen, J.Y., Cody, N.A.L., Dominguez, D., et al. (2020). A large-scale binding and functional map of human RNA-binding proteins. *Nature* **583**, 711–719.
- VanderSluis, B., Hess, D.C., Pesyna, C., Krumholz, E.W., Syed, T., Szappanos, B., Nislow, C., Papp, B., Troyanskaya, O.G., Myers, C.L., and Caudy, A.A. (2014). Broad metabolic sensitivity profiling of a prototrophic yeast deletion collection. *Genome Biol.* **15**, R64.
- Visanji, N.P., Wislet-Gendebien, S., Oschipok, L.W., Zhang, G., Aubert, I., Fraser, P.E., and Tandon, A. (2011). Effect of Ser-129 phosphorylation on interaction of  $\alpha$ -synuclein with synaptic and cellular membranes. *J. Biol. Chem.* **286**, 35863–35873.
- Warburg, O. (1924). Über den Stoffwechsel der Carcinomzelle. *Naturwissenschaften* **12**, 1131–1137.
- Webby, C.J., Wolf, A., Gromak, N., Dreger, M., Kramer, H., Kessler, B., Nielsen, M.L., Schmitz, C., Butler, D.S., Yates, J.R., 3rd, et al. (2009). Jmjd6 catalyses lysyl-hydroxylation of U2AF65, a protein associated with RNA splicing. *Science* **325**, 90–93.
- Yin, Y., Lu, J.Y., Zhang, X., Shao, W., Xu, Y., Li, P., Hong, Y., Cui, L., Shan, G., Tian, B., et al. (2020). U1 snRNP regulates chromatin retention of noncoding RNAs. *Nature* **580**, 147–150.
- Zhang, J., Lieu, Y.K., Ali, A.M., Penson, A., Reggio, K.S., Rabadan, R., Raza, A., Mukherjee, S., and Manley, J.L. (2015). Disease-associated mutation in SRSF2 misregulates splicing by altering RNA-binding affinities. *Proc. Natl. Acad. Sci. USA* **112**, E4726–E4734.

## STAR★METHODS

### KEY RESOURCES TABLE

REAGENT or RESOURCE	SOURCE	IDENTIFIER
<b>Antibodies</b>		
Actin (AC40)	Sigma	Cat # A4700 ; RRID: AB_476730
Actin (EPR16769)	Abcam	Cat # ab179467 ; RRID: AB_2737344
Anti-SC35 [SC-35]	Abcam	Cat # ab11826 ; RRID: AB_298608
COX1	Abcam	Cat # ab14705 ; RRID AB_2084810
Enolase-1	Cell Signaling Technology	Cat # 3810 ; RRID AB_2246524
FLAG M2	Sigma	Cat # F1804; RRID: RRID: AB_262044
Goat Anti-Mouse IgG H&L (Alexa Fluor® 488)	Abcam	Cat # ab150113; RRID AB_2576208
Goat Anti-Rabbit IgG H&L (Alexa Fluor® 647)	Abcam	Cat # ab150079; RRID AB_2722623
Hexokinase II (C64G5) Rabbit mAb	Cell Signaling Technology	Cat # 2867; RRID AB_2232946
HRP-linked anti-mouse IgG	GE Healthcare	Cat # NA934; RRID: AB_772206
HRP-linked anti-rabbit IgG	GE Healthcare	Cat # NXA931; RRID: AB_772209
Human OXPHOS cocktail (ATP5A, SDHB, UQCRC2, COX2, NDUFB8)	Abcam	Cat # ab110411 ; RRID: AB_2756818
IRDye 680RD Goat anti-Mouse IgG (H + L)	LI-COR Biosciences	Cat # 926-68070; RRID: AB_10956588
IRDye 680RD Goat anti-Rabbit IgG (H + L)	LI-COR Biosciences	Cat # 926-68071; RRID: AB_10956166
IRDye 800CW Goat anti-Mouse IgG (H + L)	LI-COR Biosciences	Cat # 926-32210; RRID: AB_621842
IRDye 800CW Goat anti-Rabbit IgG (H + L)	LI-COR Biosciences	Cat # 926-32211; RRID: AB_621843
LUC7L (43-I)	Santa Cruz	Cat # 101075 ; RRID: AB_2139473
LUC7L2	Sigma	Cat # HPA051631 ; RRID: AB_2681558
LUC7L3	Sigma	Cat # HPA018484 ; RRID: AB_1847248
NDUFS3	ThermoFisher Scientific	Cat # 15066-1-AP ; RRID: AB_2151109
PFKM	Abcam	Cat # ab97353 ; RRID: AB_10680060
PKP (D4B2) Rabbit mAb	Cell Signaling Technology	Cat # 8164; RRID AB_2713957
PGAM1 (D3J9T) Rabbit mAb	Cell Signaling Technology	Cat # 12098 ; RRID AB_2736922
SLC7A11 (D2M7A)	Cell signaling	Cat # 12691 ; RRID: AB_2687474
TOMM20	Santa Cruz	Cat # SC-11415 ; RRID: AB_2207533
TUBB	ThermoFisher Scientific	Cat # MA5-16308 ; RRID: AB_2537819
<b>Chemicals, peptides, and recombinant proteins</b>		
2-Deoxy-D-glucose	Sigma	Cat # D8375
Agilent Seahorse XF Base Medium	Agilent	Cat # 03334-100
Ambion RNase I, cloned, 100 U/ $\mu$ L	Ambion	Cat # AM2295
Anti-FLAG® M2 Magnetic Beads	Sigma	Cat # M8823
Antimycin A	Sigma	Cat # A8674
Carbonyl cyanide 3-chlorophenylhydrazone	Sigma	Cat # C2759
Chloramphenicol	Sigma	Cat # C0378
Coomassie Brilliant Blue R-250 Staining Solution	Biorad	Cat # 1610436
Cycloheximide	Sigma	Cat # C4859
DMEM, high glucose, pyruvate	ThermoFisher Scientific	Cat # 11995073
DMEM, no glucose, no glutamine, no phenol red	ThermoFisher Scientific	Cat # A1443001
Dulbecco's PBS	Sigma	Cat # D8537
Endo-Porter (PEG)	Gene Tools	Cat # OT-EP-PEG-1
ExoSAP-IT PCR Product Cleanup Reagent	ThermoFisher Scientific	Cat # 78201.1.ML
EXPRESS [35S]-protein labeling mix	Perkin Elmer	Cat # NEG772
Fetal Bovine Serum	ThermoFisher Scientific	Cat # 26140079

(Continued on next page)

**Continued**

REAGENT or RESOURCE	SOURCE	IDENTIFIER
Fetal Bovine Serum, dialyzed	ThermoFisher Scientific	Cat # 26400044
FLAG peptide	Sigma	Cat # F3290
FluorSave	EMD Millipore	Cat # 345789
G-418 solution	ThermoFisher Scientific	Cat # 10131035
Galactose	Sigma	Cat # G5388
Glucose	Sigma	Cat # G7021
Hoescht 33342	ThermoFisher Scientific	Cat # H1399
Pierce 16% Formaldehyde (w/v), Methanol-free	ThermoFisher Scientific	Cat # 28906
L-Glutamine	ThermoFisher Scientific	Cat # 25030081
M-MLV Reverse Transcriptase	Promega	Cat # M1701
Meclizine dihydrochloride	Sigma	Cat # SML0950
met/cys-free DMEM	ThermoFisher Scientific	Cat # 21013024
Metformin / 1,1-Dimethylbiguanide HCl	Sigma	Cat # D150959
NEBNext® Ultra II Q5® Master Mix	New England BioLabs	Cat # M0544
Odyssey Blocking Buffer	LI-COR Biosciences	Cat # 927-40000
Odyssey® Blocking Buffer (PBS)	LI-COR Biosciences	Cat # 927-40100
Oligomycin A	Sigma	Cat # 75351
Penicillin-Streptomycin	ThermoFisher Scientific	Cat # 15140122
Protease Inhibitor Cocktail (100X)	Cell Signaling	Cat # 5871
Proteinase K, Molecular Biology Grade	New England BioLabs	Cat # P8107
Puromycin Dihydrochloride	ThermoFisher Scientific	Cat # A1113803
RNase-Free DNase Set	QIAGEN	Cat # 79254
RNaseA	Takara	Cat # 740505
RNaseOUT Recombinant Ribonuclease Inhibitor	ThermoFisher Scientific	Cat # 10777019
Sulfasalasine	Sigma	Cat # S0883
T4 Polynucleotide Kinase	New England BioLabs	Cat # M0201
T4 RNA Ligase 1 (ssRNA Ligase)	New England BioLabs	Cat # M0204
Universal Nuclease (Pierce)	ThermoFisher Scientific	Cat # 88702
Uridine	Sigma	Cat # U3003
XBridge BEH Amide column	Water	Cat # 186006091
ZIC-philic column	Merck	Cat # 150460

**Critical commercial assays**

Amplex red glutamic acid/glutamate oxidase assay kit	ThermoFisher Scientific	Cat # A22189
Citrate Synthase Activity Assay Kit	Abcam	Cat # ab119692
DC Protein Assay	Biorad	Cat # 5000112
Glycogen Assay Kit II (Colorimetric)	Abcam	Cat # ab169558
Hoechst 33342, Trihydrochloride, Trihydrate	ThermoFisher Scientific	Cat # H3570
NativeMark Unstained Protein Standard	ThermoFisher Scientific	Cat # LC0725
NativePAGE 3 to 12%, Bis-Tris, 1.0 mm, Mini Protein Gel, 10-well	ThermoFisher Scientific	Cat # BN1001BOX
NativePAGE Cathode Buffer Additive (20X)	ThermoFisher Scientific	Cat # BN2002
NativePAGE Running Buffer (20X)	ThermoFisher Scientific	Cat # BN2001
NativePAGE Sample Buffer (4X)	ThermoFisher Scientific	Cat # BN2003
Novex 10–20% Tris-Glycine Mini Gels	ThermoFisher Scientific	Cat # XP10200BOX
Novex 4–12% Tris-Glycine Mini Gels	ThermoFisher Scientific	Cat # XP04122BOX
Precision Plus Protein Kaleidoscope Prestained Protein Standards	Biorad	Cat # 1610375
RNeasy Mini Kit	QIAGEN	Cat # 74106
Seahorse XFe96 FluxPaks	Agilent	Cat # 102416-100

(Continued on next page)

**Continued**

REAGENT or RESOURCE	SOURCE	IDENTIFIER
Trans-Blot Turbo Midi Nitrocellulose Transfer Packs	Biorad	Cat # 1704159
LUC7L Taqman Assay	ThermoFisher Scientific	Hs00216077
LUC7L2 Taqman Assay	ThermoFisher Scientific	Hs00255388
LUC7L3 Taqman Assay	ThermoFisher Scientific	Hs00895240
SLC7A11 Taqman Assay	ThermoFisher Scientific	Hs00921938
TBP Taqman Assay	ThermoFisher Scientific	Hs00427620
<b>Deposited data</b>		
RNA-seq	GEO	GEO: GSE157917
Proteomics	PRIDE	PRIDE: PXD021917
<b>Experimental models: cell lines</b>		
K562	ATCC	CCL-243
293T	ATCC	CRL-3216
HAP1	Horizon Discovery	C631
HeLa	ATCC	CCL-2
<b>Oligonucleotides</b>		
ACIN1_sg1_as	Integrated DNA Technologies	AAACCAGAGATGCGAGAGTCATCAC
ACIN1_sg1_s	Integrated DNA Technologies	CACCGTGATGACTCTGCATCTCTG
ACIN1_sg2_as	Integrated DNA Technologies	AAACCCCTCTGTGTCAGTGTCTTTCC
ACIN1_sg2_s	Integrated DNA Technologies	CACCGGAAACAGTGACACAGAGGG
AluYb8_as	Integrated DNA Technologies	GAGACGGAGTCTCGCTCTGTC
AluYb8_probe	Integrated DNA Technologies	VIC-ACTGCAGTCCGCAGTCGGCCT-MGBNFQ
AluYb8_s	Integrated DNA Technologies	CTTGCAGTGAGGCCGAGATT
ENO1_sg1_as	Integrated DNA Technologies	AAACTGAAGTTGCTGCACCGACTC
ENO1_sg1_s	Integrated DNA Technologies	CACCGAGTCGGTGCAGCAAACCTCA
ENO1_sg2_as	Integrated DNA Technologies	AAACAGTGGCTCTCAACTGGTATC
ENO1_sg2_s	Integrated DNA Technologies	CACCGATAACCAGTTGAAGCACCAC
HK2_sg1_as	Integrated DNA Technologies	AAACCGCCTTGTCTCCTTGATGC
HK2_sg1_s	Integrated DNA Technologies	CACCGCATCAAGGAGAACAAAGGCG
HK2_sg2_as	Integrated DNA Technologies	AAACTGTGTTGGGTGAAAGTAAC
HK2_sg2_s	Integrated DNA Technologies	CACCGTTACTTCACCCAAAGCACA
HNRNPD_sg1_as	Integrated DNA Technologies	AAACCGTTCTACTGGCGTCATC
HNRNPD_sg1_s	Integrated DNA Technologies	CACCGATTGACGCCAGTAAGAACG
HNRNPD_sg2_as	Integrated DNA Technologies	AAACCCGAAGTGCCTCCGACATC
HNRNPD_sg2_s	Integrated DNA Technologies	CACCGATGTGGAGGAGCAGTCGG
LUC7L_sg1_as	Integrated DNA Technologies	AAACCAAGTGAACCTGCCACCGAC
LUC7L_sg1_s	Integrated DNA Technologies	CACCGTCGGTGGCAAGTTACACTG
LUC7L_sg2_as	Integrated DNA Technologies	AAACAGTCGGATTTGGTACATC
LUC7L_sg2_s	Integrated DNA Technologies	CACCGATGTACCAAAATCCACGACT
LUC7L2_sg1_as	Integrated DNA Technologies	AAACCTCTTAAAGCCAGGTACATGG
LUC7L2_sg1_s	Integrated DNA Technologies	CACCGCCATGACCTGGCTTAAGAG
LUC7L2_sg2_as	Integrated DNA Technologies	AAACTTACTTCTGGGATTCCTCC
LUC7L2_sg2_s	Integrated DNA Technologies	CACCGGAGGAATCCCAGAAAGTAA
LUC7L3_sg1_as	Integrated DNA Technologies	AAACCGTCTGATCCTACGTTCTAC
LUC7L3_sg1_s	Integrated DNA Technologies	CACCGTAGAACGTAGGATCAGACG
LUC7L3_sg2_as	Integrated DNA Technologies	AAACCGAGAGCGTAAGTCCCGCGGC
LUC7L3_sg2_s	Integrated DNA Technologies	CACCGCCGCGGGACTTACGCTCTCG
ND2_as	Integrated DNA Technologies	CCTGCAAAGATGGTAGAGTAGATGA
ND2_probe	Integrated DNA Technologies	FAM-CCCTGGCCCCAACCC-MGBNFQ
ND2_s	Integrated DNA Technologies	TGTTGGTTATCCCTCCGTACTA

(Continued on next page)

**Continued**

REAGENT or RESOURCE	SOURCE	IDENTIFIER
NDUFB5_sg1_as	Integrated DNA Technologies	AAACAAACTCTGGAATTCTGCTAGTC
NDUFB5_sg1_s	Integrated DNA Technologies	CACCGAACTAGCAGAAATTCCAGA
NDUFB5_sg2_as	Integrated DNA Technologies	AAACAAACTCTTGATATGGGATGCTACAC
NDUFB5_sg2_s	Integrated DNA Technologies	CACCGTAGCATCCCATATCAAGA
PABPC1_sg1_as	Integrated DNA Technologies	AAACCTTTCTGAGCTGACACCAC
PABPC1_sg1_s	Integrated DNA Technologies	CACCGTGGTCGAGCTCAGAAAAAGG
PABPC1_sg2_as	Integrated DNA Technologies	AAACCTCTGGGCTACCGTATGC
PABPC1_sg2_s	Integrated DNA Technologies	CACCGCATACCGTAGCCCAAGGAG
PFKM_exon12_5SS Antisense Oligonucleotide	Gene Tools	GGCCACACAGCCCAGTGACTTACCA
PFKM_RT_as	Integrated DNA Technologies	TCATGGAATGTGTCAGGTG
PFKM_RT_s	Integrated DNA Technologies	CATCATCATTGTCAGGTG
PFKM_RT2_as	Integrated DNA Technologies	ACACATCCATGAGGGCAG
PFKM_RT2_s	Integrated DNA Technologies	CCGTGGTCTCGTCTCAACA
PFKP_sg1_as	Integrated DNA Technologies	AAACCCGAGAGTTGACACACATC
PFKP_sg1_s	Integrated DNA Technologies	CACCGATGTGTCAAACTCTCGG
PFKP_sg2_as	Integrated DNA Technologies	AAACTGGGATCTGATCATCCGGC
PFKP_sg2_s	Integrated DNA Technologies	CACCGCCGGATGATCAGATCCCAA
PGAM1_sg1_as	Integrated DNA Technologies	AAACACCTGAGGCCGGCGGGCAC
PGAM1_sg1_s	Integrated DNA Technologies	CACCGTGGCCGCCGGCTAGGT
PGAM1_sg2_as	Integrated DNA Technologies	AAACCTGAAGCGGTTCTCCAGGTT
PGAM1_sg2_s	Integrated DNA Technologies	CACCGAACCTGGAGAACCGCTTCAG
Random Primers	ThermoFisher Scientific	Cat # 48190011
SLC7A11_exon7_5SS Antisense Oligonucleotide	Gene Tools	CCAACCTGGACTTACCACTGCCACT
SLC7A11_exon9_5SS Antisense Oligonucleotide	Gene Tools	ATATACTGTTAATATGCATTACCA
SLC7A11_RT_as	Integrated DNA Technologies	GGCAGATTGCCAAGATCTCAAG
SLC7A11_RT_s	Integrated DNA Technologies	TGCTGGCTGGTTTACCTCAA
SNRNP70_sg1_as	Integrated DNA Technologies	AAACCCCGCTACGATGAGAGGTAAC
SNRNP70_sg1_s	Integrated DNA Technologies	CACCGTTACCTCTCATCGTAGCGGG
SNRNP70_sg2_as	Integrated DNA Technologies	AAACCTTACAAACACGCAGATGGC
SNRNP70_sg2_s	Integrated DNA Technologies	CACCGCCATCTGCGTGTGTTAAG
SNRPA_sg1_as	Integrated DNA Technologies	AAACCCGCCTTGACAGCCTTCTTC
SNRPA_sg1_s	Integrated DNA Technologies	CACCGAAGAAGGCTGTGCAAGGCGG
SNRPA_sg2_as	Integrated DNA Technologies	AAACGGCCTTGTCACTTCAAGG
SNRPA_sg2_s	Integrated DNA Technologies	CACCGGCCTTGTCACTTCAAGG
Standard Control Antisense Oligonucleotide	Gene Tools	CCTCTTACCTCAGTTACAATTATA
TPI1_sg1_as	Integrated DNA Technologies	AAACCAGTCTTGATCATGCCAGGC
TPI1_sg1_s	Integrated DNA Technologies	CACCGCCTGGCATGATAAGACTG
TPI1_sg2_as	Integrated DNA Technologies	AAACCGTGGTGGTCTGGGCAC
TPI1_sg2_s	Integrated DNA Technologies	CACCGTGGCCAGGACCACCCACG
<b>Recombinant DNA</b>		
plentiCRISPR v2	Addgene	Plasmid # 52961
pLV-EF1a-IRES-Puro	Addgene	Plasmid # 85132
pLV-EF1a-IRES-Puro GFP-3xFLAG	This study	N/A
pLV-EF1a-IRES-Puro LUC7L2-3xFLAG	This study	N/A
pLV-EF1a-IRES-Puro PFKM	This study	N/A
pMD2.G	Addgene	Plasmid # 12259
psPAX2	Addgene	Plasmid # 12260
pWPI /Neo	Addgene	Plasmid # 35385
pWPI /Neo GFP	This study	N/A

(Continued on next page)

**Continued**

REAGENT or RESOURCE	SOURCE	IDENTIFIER
pWPI /Neo LUC7L-3xFLAG	This study	N/A
pWPI /Neo LUC7L2-3xFLAG	This study	N/A
pWPI /Neo LUC7L3-3xFLAG	This study	N/A
pWPI /Neo SLC7A11-HA	This study	N/A
PLENTICRISPR_v2_PFKP_sgRNA1	To et al., 2019	N/A
PLENTICRISPR_v2_PFKP_sgRNA1	To et al., 2019	N/A
<b>Software and algorithms</b>		
ImageJ	NIH	<a href="https://imagej.nih.gov/ij/">https://imagej.nih.gov/ij/</a>
CLIPper	Yeo lab	<a href="https://github.com/YeoLab/clipper/wiki/CLIPper-Home">https://github.com/YeoLab/clipper/wiki/CLIPper-Home</a>
Clustal Omega	EMBL-EBI	<a href="https://www.ebi.ac.uk/Tools/msa/clustalo/">https://www.ebi.ac.uk/Tools/msa/clustalo/</a>
Gene Ontology GOrilla	Eden et al., 2009	<a href="http://cbl-gorilla.cs.technion.ac.il/">http://cbl-gorilla.cs.technion.ac.il/</a>
Gene set enrichment analysis (GSEA)	Broad Institute	<a href="https://www.gsea-msigdb.org/gsea/index.jsp">https://www.gsea-msigdb.org/gsea/index.jsp</a>
IGV	Broad Institute	<a href="https://software.broadinstitute.org/software/igv/">https://software.broadinstitute.org/software/igv/</a>
MAGECK	Li et al., 2014	<a href="https://sourceforge.net/p/mageck/wiki/Home/">https://sourceforge.net/p/mageck/wiki/Home/</a>
Prism	GraphPad	<a href="https://www.graphpad.com/scientific-software/prism/">https://www.graphpad.com/scientific-software/prism/</a>
rMATS	Shen et al., 2014	<a href="http://rnaseq-mats.sourceforge.net/">http://rnaseq-mats.sourceforge.net/</a>
Seahorse Wave Desktop Software	Agilent	<a href="https://www.agilent.com/en/product/cell-analysis-real-time-cell-metabolic-analysis/xf-software/seahorse-wave-desktop-software-740897">https://www.agilent.com/en/product/cell-analysis-real-time-cell-metabolic-analysis/xf-software/seahorse-wave-desktop-software-740897</a>
STAR	Dobin et al., 2013	<a href="https://github.com/alexdobin/STAR">https://github.com/alexdobin/STAR</a>
Kallisto	Bray et al., 2016	<a href="https://github.com/pachterlab/kallisto">https://github.com/pachterlab/kallisto</a>
R	The R Project	<a href="https://www.r-project.org/">https://www.r-project.org/</a>
DESeq2	Love et al., 2014	<a href="https://bioconductor.org/packages/release/bioc/html/DESeq2.html">https://bioconductor.org/packages/release/bioc/html/DESeq2.html</a>

## RESOURCE AVAILABILITY

### Lead contact

Vamsi K. Mootha ([vamsi@hms.harvard.edu](mailto:vamsi@hms.harvard.edu))

### Materials availability

Further information and requests for resources and reagents should be directed to and will be fulfilled by the lead contact.

### Data and code availability

RNA sequencing data were deposited at GEO (GEO: GSE157917). Proteomics data were deposited at PRIDE (PRIDE: PXD021917). Plasmids were deposited at Addgene. Unedited gel scans are available in the supplemental information file ([Data S1](#)).

## EXPERIMENTAL MODEL AND SUBJECT DETAILS

### Cell lines

K562 (ATCC CCL-243), HeLa (ATCC CCL-2) and 293T (ATCC CRL-3216) were obtained from ATCC and were re-authenticated by STR profiling at ATCC prior submission of the manuscript. HAP1 cells were from Horizon Discovery (C631). Cells were periodically tested to ensure absence of mycoplasma.

## METHOD DETAILS

### CRISPR screen re-analysis

CRISPR screen analysis was performed either using a normalized Z-score approach ([To et al., 2019](#)) or using MAGECK ([Li et al., 2014](#)). Raw sgRNA read counts were normalized to reads per million and then log<sub>2</sub> transformed using the following formula: Log<sub>2</sub>(reads from an individual sgRNA / total reads in the sample 10<sup>6</sup> + 1) ([To et al., 2019](#)). Log<sub>2</sub> fold-change of each sgRNA was

determined relative to the pre-swap control. For each gene in each replicate, the mean  $\log_2$  fold-change in the abundance of all 4 sgRNAs was calculated. Genes with low expression ( $\log_2$  FPKM < 0) according to publicly available K562 RNA-seq dataset (sample GSM854403 in GEO series GEO: GSE34740) and essential genes previously reported (Arroyo et al., 2016) were removed. Log<sub>2</sub> fold-changes were averaged by taking the mean across replicates. For each treatment, a null distribution was defined by the 3,726 genes with lowest expression. To score each gene within each treatment, its mean  $\log_2$  fold-change across replicates was Z-score transformed, using the statistics of the null distribution defined as above. To score each gene using MAGeCK, normalized sgRNA read counts from the duplicate in each condition were used as input for MAGeCK v0.5.3 to obtain a p value and FDR for gene enrichment or depletion relative to the reference samples (pre-swap). MAGeCK was run with default parameters. For representation purpose, viability in galactose was defined as the -annexin V value.

### Cell culture and cell growth assays

Unless otherwise specified, cells were maintained in DMEM containing 1mM sodium pyruvate (ThermoFisher Scientific) with 25 mM glucose, 10% fetal bovine serum (FBS, ThermoFisher Scientific), 50  $\mu$ g/mL uridine (Sigma), and 100 U/mL penicillin/streptomycin (ThermoFisher Scientific) under 5% CO<sub>2</sub> at 37°C. Cells were counted using a ViCell Counter (Beckman) and only viable cells were considered. Drugs were diluted in the same culture media for cell growth assays and compared to the solvent control (DMSO or water). For galactose growth assays, FBS was replaced by dialyzed FBS (Life Technologies) and glucose was replaced by an equivalent amount of galactose.

### Gene-specific CRISPR-Cas9 knockouts

The two best sgRNAs from the Avana-library were ordered as complementary oligonucleotides (Integrated DNA Technologies) and cloned in pLentiCRISPRv2. An sgRNA targeting EGFP was used as a negative control. Lentiviruses were produced according to Addgene's protocol (Sanjana et al., 2014) and 24h post-infection cells were selected with 2mg/mL puromycin (ThermoFisher Scientific) for 48h. Cells were then maintained in routine culture media for 10-20 addition days before analysis. Gene disruption efficiency was verified by qPCR and/or immunoblotting. For HAP1 cells, a LUC7L2<sup>KO</sup> cell line expressing LUC7L2 cDNA was used as control (LUC7L2<sup>Rescue</sup>). For acute treatment, K562 cells were transduced with a high titer of sgRNAs targeting LUC7L2 and analyzed after 7 days. Sequences of the sgRNAs used are in the [Key resources table](#).

### Antisense oligonucleotides (ASOs) treatment

2x10<sup>5</sup>/mL HAP1 cells were seeded in a culture or Seahorse plate. 24h later, the media was replaced by fresh media containing 10  $\mu$ M of the specific or control ASO, and 6  $\mu$ L/mL of PEG-based endoporter (GeneTools). Cells were analyzed 48h-72h later and recounted after the experiment.

### Oxygen consumption and extracellular acidification rates by Seahorse XF analyzer

1.25x10<sup>5</sup> K562 cells were plated on a Seahorse plate in Seahorse XF DMEM media (Agilent) containing 25mM glucose and 4mM glutamine (ThermoFisher Scientific). Oxygen consumption and extracellular acidification rates were simultaneously recorded by a Seahorse XFe96 Analyzer (Agilent) using the mito stress test protocol, in which cells were sequentially perturbed by 2mM oligomycin, 1  $\mu$ M CCCP and 0.5mM antimycin (Sigma). Data were analyzed using the Seahorse Wave Desktop Software (Agilent). Data were not corrected for carbonic acid derived from respiratory CO<sub>2</sub>. For Seahorse in HeLa and HAP1 cells, 5x10<sup>4</sup> and 1x10<sup>5</sup> cells, respectively, were plated in a 96-well seahorse plate the day before the experiment. Cells were trypsinized after the experiment and recounted and the data was normalized to cell number.

### Media acidification

To visualize media acidification, 3x10<sup>6</sup> LUC7L2<sup>WT</sup> or LUC7L2<sup>KO</sup> K562 cells were collected by centrifugation, washed in PBS and incubate in 1mL of DMEM media (containing 25mM glucose and phenol red, a pH indicator) for 3h before imaging.

### Mitochondrial and nuclear DNA determination

Mitochondrial and nuclear DNA determination was carried as previously described (Bao et al., 2016). LUC7L2<sup>WT</sup> and LUC7L2<sup>KO</sup> K562 cells were grown for 24h in fresh cell culture media and counted. 1x10<sup>5</sup> cells from each condition (n = 3) were harvested and lysed in 100  $\mu$ L mtDNA lysis buffer (25mM NaOH, 0.2mM EDTA) before incubation at 95°C for 15min. 100  $\mu$ L of 40mM Tris-HCl pH 7.5 was added to neutralize the reaction on ice. Samples were diluted 50x and the ratio between mitochondrial and nuclear DNA was determined using a custom Taqman based assay and qPCR using a CFX96 quantitative PCR machine (Biorad). Relative mtDNA abundance was determine using the  $\Delta\Delta Ct$  method.

### RNA extraction, reverse transcription, and qPCR

qPCR was performed using the TaqMan assays (ThermoFisher Scientific). RNA was extracted from total cells with an RNeasy kit (QIAGEN) and DNase-I digested before murine leukemia virus (MLV) reverse transcription using random primers (Promega) and a CFX96 quantitative PCR machine (rad). All data were normalized to TBP using  $\Delta\Delta Ct$  method.

### Citrate synthase activity determination

Citrate synthase activity was determined using a commercially available kit (Abcam). *LUC7L2<sup>WT</sup>* and *LUC7L2<sup>KO</sup>* K562 cells were grown for 48h in fresh cell culture media and counted.  $5 \times 10^6$  cells from each condition ( $n = 3$ ) were harvested, washed in PBS and resuspended in lysis buffer (provided by the kit) and completed with protease inhibitor. 100 $\mu$ L of lysate was used and the experiment was performed as described in the kit protocol. Protein abundance was determined using a DC protein assay (Biorad) and the citrate synthase activity signal was normalized to the protein abundance of each sample.

### Glycogen determination

Glycogen synthase activity was determined using a commercially available kit (Abcam). *LUC7L2<sup>WT</sup>* and *LUC7L2<sup>KO</sup>* K562 cells were grown for 24h in fresh cell culture media and counted.  $1 \times 10^6$  cells from each condition ( $n = 8$ ) were incubated in fresh media for another 6h before being harvested, washed in ice-cold PBS and resuspended in lysis buffer (provided by the kit). 25 $\mu$ L of lysate was used and the experiment was performed as described in the kit protocol and normalized to total protein abundance.

### Glutamate determination

Glutamate levels were determined using a commercially available AMPLEX kit (Life Technologies). *LUC7L2<sup>WT</sup>*, *LUC7L2<sup>Rescue</sup>* (*LUC7L2<sup>KO</sup>* cells were a *LUC7L2* cDNA was stably expressed), *LUC7L2<sup>KO</sup>* and ASO treated K562 or HAP1 cells were grown for 24h in fresh culture media and counted. Cells were then washed with PBS, the media was replaced and the cells were incubated for another 3h. Medias were then collected and centrifuged at 2,000 g for 3min, and glutamate concentrations were determined from the supernatant.

### Cell viability assay in galactose

To measure viability in galactose, cells were washed in PBS, counted and an equal number of cells was seeded in culture media containing 25mM glucose or 25mM galactose. 24h later, cells were collected and viable cells were determined using a Vi-Cell Counter (Beckman).

### Electron microscopy

Electron microscopy was performed at the Keck Microscopy Facility at Whitehead.  $5 \times 10^6$  *LUC7L2<sup>WT</sup>* and *LUC7L2<sup>KO</sup>* K562 cells were grown for 24h in fresh cell culture media and were fixed in 2.5% gluteraldehyde, 3% paraformaldehyde with 5% sucrose in 0.1M sodium cacodylate buffer (pH 7.4), pelleted, and post fixed in 1% OsO<sub>4</sub> in veronal-acetate buffer. Cells were stained *en block* overnight with 0.5% uranyl acetate in veronal-acetate buffer (pH6.0), dehydrated and embedded in Embed-812 resin. Sections were cut on a Leica EM UC7 ultra microtome with a Diatome diamond knife at a thickness setting of 50 nm, stained with 2% uranyl acetate, and lead citrate. The sections were examined using a FEI Tecnai spirit at 80KV and photographed with an AMT CCD camera.

### Confocal microscopy and immunofluorescence

HeLa cells were transduced with pWPI-LUC7L2-GFP at least 48h before the experiment and grown on coverslips until 30%–50% confluent. Cells were successively fixed in 4% paraformaldehyde in cell culture media at room temperature for 30min, blocked/permeabilized for 30min in Abdiril buffer (PBS + 0.1% Triton X-100 + 3% bovine serum albumin (w/v)), incubated with primary antibodies (1:200) in Abdiril buffer for 1h, washed 3x 5min in PBS + 0.1% Triton X-100, incubated in fluorophore-coupled secondary antibodies (1:1000) and hoescht (1:10000) in Abdiril for 30min, washed 3x in PBS + 0.1% Triton X-100 and mounted on a slide using FluorSave (EMD Millipore). Cells were imaged using a Zeiss LSM700 confocal microscope

### Polyacrylamide gel electrophoresis and immunoblotting

Cells were harvested, washed in PBS and lysed for 5min on ice in RIPA buffer (25mM Tris pH 7.5, 150mM NaCl, 0.1% SDS, 0.1% sodium deoxycholate, 1% NP40 analog, 1x protease (Cell Signaling) and 1:500 Universal Nuclease (ThermoFisher Scientific)). Protein concentration was determined from total cell lysates using DC protein assay (Biorad). Gel electrophoresis was done on Novex Tris-Glycine gels (ThermoFisher Scientific) before transfer using the Trans-Blot Turbo blotting system and nitrocellulose membranes (Biorad). All immunoblotting was performed in Intercept Protein blocking buffer (Li-Cor). Washes were done in TBS + 0.1% Tween-20 (Sigma). Specific primary antibodies were diluted 1:100-1:5000 in blocking buffer. Fluorescent-coupled secondary antibodies were diluted 1:10,000 in blocking buffer. Membranes were imaged with an Odyssey CLx analyzer (Li-Cor) or by chemiluminescence. In a few instances, the same lysates were loaded on parallel gels to avoid antibody cross-reactivity, or because the proteins of interest could not be resolved on the same percentage gels. In these cases, a loading control is provided for all gels, and panels from the same immunoblots are connected with a dotted line on the figure. All raw immunoblots pictures are provided in the supplemental information document.

### Liquid chromatography-mass spectrometry (LC-MS)

#### Intracellular metabolite profiling

*LUC7L2<sup>WT</sup>* and *LUC7L2<sup>KO</sup>* K562 cells were pre-incubated overnight in profiling media containing glucose-free DMEM media (ThermoFisher Scientific), 10% dialyzed FBS (ThermoFisher Scientific), penicillin and streptomycin (ThermoFisher Scientific) and

25mM glucose (Sigma) but omitting supplemental pyruvate or uridine. On the day of the experiment,  $2.5 \times 10^6$  cells were seeded in 3mL of profiling media in a 6-well plate ( $n = 6$  replicate plates for each genotype). An additional well containing 3mL of media but no cells was included as control. After 8h of incubation, cells were centrifuged at 300 g for 3min at room temperature and the culture media was saved and frozen at  $-80^{\circ}\text{C}$  until further analysis (described below). The cell pellet was briefly washed in ice-cold 150mM NaCl and centrifuged again. 1mL dry ice-cold 80% methanol was then added to quench metabolism. Cells were incubated on ice for > 20min, centrifuged at 20,000 g ( $4^{\circ}\text{C}$ ) and the supernatant was saved and dried down in a speed vacuum concentrator (Savant SPD 1010, ThermoFisher Scientific) and stored at  $-80^{\circ}\text{C}$  until analysis. On the day of analysis, samples were re-suspended in 120 $\mu\text{L}$  of 60/40 acetonitrile/water, vortexed, sonicated in ice-cold water for 1min, incubated on ice for 20min and the supernatant was collected in an autosampler vial after centrifugation at 21,000 g for 20min at  $4^{\circ}\text{C}$ . Pooled quality control (PooledQC) samples were generated by combining  $\sim 20\mu\text{L}$  of each sample. Metabolite profiling was performed using a Dionex Ultimate 3000 UHPLC system coupled to a Q-Exactive Plus orbitrap mass spectrometer (ThermoFisher Scientific, Waltham, MA) with an Ion Max source and HESI II probe operating in polarity switching mode. A zwitterionic zic pHilic column (150  $\times$  2.1mm, 5 $\mu\text{m}$ , Merck KGaA) was used for polar metabolite separation. Mobile phase A (MPA) was 20mM ammonium carbonate in water, pH9.6 (adjusted with ammonium hydroxide) and MPB was acetonitrile. The column was held at  $27^{\circ}\text{C}$ , with an injection volume of 5 $\mu\text{L}$ , and an autosampler temperature of  $4^{\circ}\text{C}$ . The LC conditions at a flow rate of 0.15 mL/min were: 0min: 80% B, 0.5min: 80% B, 20.5min: 20% B, 21.3min: 20% B, 21.5min: 80% B with 7.5min of column equilibration time. MS parameters were: sheath gas flow = 30, aux gas flow = 7, sweep gas flow = 2, spray voltage = 2.80 for negative & 3.80 for positive ion modes, capillary temperature =  $310^{\circ}\text{C}$ , S-lens RF level = 50 and aux gas heater temp  $370^{\circ}\text{C}$ . Data acquisition was performed using Xcalibur 4.1 (ThermoFisher Scientific) in full scan mode with a range of 70-1000 m/z, a resolving power of 70,000, an AGC target of  $1 \times 10^6$ , and a maximum injection time of 80ms. Data analysis was done using Compound Discoverer 3.0. Samples were injected in a randomized order and pooled QC samples were injected regularly throughout the analytical batches. Metabolite annotation was based on accurate mass ( $\pm 5\text{ppm}$ ) and matching retention time ( $\pm 0.3\text{min}$ ) as well as MS/MS fragmentation pattern from the pooled QC samples against in-house retention time +MSMS library of reference chemical standards. Metabolites which had a pooled QC CV < 20% were used for the statistical analysis.

#### Media profiling

30 $\mu\text{L}$  of control or spent media was mixed with 120 $\mu\text{L}$  of ice-cold acetonitrile containing the metabolomics amino acid mix from Cambridge Isotope Labs (MSK-A2-1.2),  $^{13}\text{C}_6$ -glucose,  $^{13}\text{C}_3$ -pyruvate, and  $^{13}\text{C}_3$ -lactate as internal standards, was vortexed, incubated on ice for 20min, centrifuged at 21,000 g for 20min at  $4^{\circ}\text{C}$  and the supernatant was transferred to an autosampler vial for LC-MS analysis. Calibration curves were prepared in water at varying concentration levels depending on the amino acid level in the DMEM media formulation. Metabolite separation was done using XBridge BEH amide (2.1 $\times$ 150mm, 1.7  $\mu\text{m}$ , Waters Corporation, MA). Mobile phase A was 90/5/5 water/acetonitrile/methanol, 20mM ammonium acetate, 0.2% acetic acid and mobile phase B was 90/10 acetonitrile/water, 10mM ammonium acetate, 0.2% acetic acid. The column temperature was  $40^{\circ}\text{C}$  and flow rate was 0.3 mL/min. The chromatographic gradient was: 0min: 95% B, 9min: 70% B, 9.75min: 40% B, 12min: 40% B, 13min: 30% B, 14min: 30% B, 14.1min: 10% B, 17min: 95% B, 22min: 95% B. MS parameters were: sheath gas flow = 50, aux gas flow = 12, sweep gas flow = 2, spray voltage = 2.80 for negative (3.50 for positive), Capillary temperature =  $320^{\circ}\text{C}$ , S-lens RF level = 50 and aux gas heater temperature  $380^{\circ}\text{C}$ . Data acquisition was done using Xcalibur 4.1 (ThermoFisher Scientific) and performed in full scan mode with a range of 70-1000 m/z, a resolving power of 70,000, an AGC target  $10^6$ , and a maximum injection time of 100ms. Tracefinder 4.1 was used for quantitation analysis. One  $\text{LUC7L2}^{KO}$  sample gave aberrant spectra and was excluded.

#### LUC7L2-3xFLAG immunoprecipitation and mass spectrometry

For immunoprecipitation, a 3xFLAG-tagged version of LUC7L2 was cloned into pWPI-Neo (Addgene), and viruses were produced. pWPI-GFP served as control. 293T cells were infected and expanded for at least 48h. An equal number of cells from each condition in duplicate was lysed in IP lysis buffer (50 mM Tris/HCl (pH 7.5), 150 mM NaCl, 1 mM MgCl<sub>2</sub>, 1% NP-40, 0.1% sodium deoxycholate, 1  $\times$  protease (Cell Signaling)). Lysates were cleared by centrifugation at 20,000 g for 20min and the supernatants were saved. Washed FLAG M2 magnetic beads (Sigma) were added to the lysate and incubated overnight at  $4^{\circ}\text{C}$ . Beads were recovered after extensive washing, and the protein/RNA complexes were eluted with 100  $\mu\text{g}/\text{mL}$  3xFLAG peptide (Sigma). For protein isolation, the eluate was run on an SDS-PAGE gel until the whole lysate entered the gel. Single bands containing all proteins from the sample were then cut and analyzed by mass spectrometry at the Whitehead proteomics facility. Peptides were identified and quantified using the Top 3 total ion current (TIC) method (Scaffold4). Interacting proteins were considered positive when they were enriched > 2-fold over either control and identified only by unique peptides.

#### Enhanced crosslinking and immunoprecipitation (eCLIP)

Libraries were generated using standard eCLIP methods according to published protocols (Van Nostrand et al., 2017). In brief, K562 and HeLa cells ( $2 \times 10^7$  for each replicate plate) were UV crosslinked (254 nm, 400 mJ/cm<sup>2</sup>), then lysed and sonicated (Bioruptor) in eCLIP lysis buffer (50 mM Tris-HCl pH 7.4, 100 mM NaCl, 1% NP-40 (Igepal CA630), 0.1% SDS, 0.5% sodium deoxycholate, 1:200 Protease Inhibitor Cocktail I, in RNase/DNase-free H<sub>2</sub>O). RNA fragments were created by incubating lysates with RNase I (Ambion) and LUC7L2:RNA complexes were immunoprecipitated for 2h at  $4^{\circ}\text{C}$  using Dynabeads bound to 4  $\mu\text{g}$  of LUC7L2-specific affinity-purified antibody. In parallel, libraries were generated from size-matched input (SMLInput) samples containing RNAs present in the whole cell lysates, i.e., sans RBP-specific IP. For the IPs, a series of stringent washes (high salt wash buffer: 50 mM Tris-HCl

pH 7.4, 1 M NaCl, 1 mM EDTA, 1% NP-40, 0.1% SDS, 0.5% sodium deoxycholate, in RNase/DNase-free H<sub>2</sub>O; wash buffer: 20 mM Tris-HCl pH 7.4, 10 mM MgCl<sub>2</sub>, 0.2% Tween-20, in RNase/DNase-free H<sub>2</sub>O) was followed by RNA dephosphorylation with FastAP (ThermoFisher Scientific) and T4 PNK (NEB) then ligation of an adaptor to the 3' ends of the RNAs with T4 RNA ligase 1 (NEB). Protein:RNA complexes were separated on 4%-12% polyacrylamide gels, transferred to a nitrocellulose membranes and RNA was extracted from the membranes using Proteinase K (NEB). Immunoprecipitation was confirmed by parallel western blotting of fractions of each sample with the antibody described previously. Following purification, SMIInput RNA were dephosphorylated and 3'-ligated and all samples were reverse transcribed with Superscript III (Invitrogen). Free primers were removed with ExoSap-IT (Affymetrix) and a DNA adaptor was ligated to the 3' ends of the cDNA with T4 RNA ligase 1. cDNA was quantified by qPCR and PCR amplified using Q5 Master Mix (NEB) and resulting libraries were purified prior to Illumina sequencing.

Blue-native PAGE

For blue-native PAGE, a mitochondria-rich fraction (Jourdain et al., 2013) was isolated from *LUC7L2*<sup>WT</sup> and *LUC7L2*<sup>KO</sup> K562 and HeLa cells grown for two weeks in glucose or galactose-containing by differential centrifugation. An equal amount of mitochondria were resuspended in blue-native loading buffer containing 1% digitonin (Life Technologies) before electrophoresis on a 3 to 12% Native PAGE (Life Technologies) according to the manufacturer's instruction. Gels were then fixed and stained with Coomassie R-250, or transferred to PVDF membranes, denatured by 3% acetic acid treatment, destained with methanol, blocked and an immunodetection was performed with the indicated antibodies and secondary HRP-coupled antibodies. Samples were loaded on parallel gels to avoid cross-reactivity between antibodies.

## Mitochondrial translation

Determination of mitochondrial translation products in *LUC7L2<sup>WT</sup>* and *LUC7L2<sup>KO</sup>* cells was performed as previously described (Jourdain et al., 2013). K562s cells were incubated for 20 min in methionine/cysteine-free DMEM (Sigma) complemented with dialyzed serum and 2mM L-glutamine. Cells were then incubated for 1h in the same medium in the presence of 100 µg/ml emetine and 100 µCi/µL <sup>35</sup>S-labeled methionine/cysteine (PerkinElmer). Total protein concentration of cell lysates was measured, and lysates were resolved on an acrylamide gel, transferred to a nitrocellulose membrane, and analyzed by autoradiography. A mitochondrial translation inhibitor (chloramphenicol) was used as a control.

## Gene-specific cDNA cloning and expression

cDNAs of interest were custom designed (Genewiz or IDT) and cloned into pWP1-Neo or pLV-lenti-puro (Visanji et al., 2011; Hayer et al., 2016) using BamHI/Spel and BamHI/NotI (NEB), respectively. cDNA sequences were:

### **GFP-3xFLAG**

atgttgagcaaggcgaggagctgttccacgggggtggccatcctggcgactggacggcgacgtaaacggccacaagttagtcggtccggcgagggcgagggcgat  
gcccacccatcgcaagctgaccctgaagtcatctgcaccacccggcaagctgccccgtgccctggcccccacccctgtgaccacccctgactacggcgatcgcttcagccgta  
cccccacccatcgcaagctgaccacactctcaagtgcccatgcccggactgtccaggagcgaccatcttcaaggacgcacggcaactacaagacccgcggag  
gtgaagttcgagggcgacaccctgttgaaccgcatacgactgaaggcatcgacttcaaggaggacgcacatcttgggcaacatctgggcaactggagtacaactacaacacc  
acgttatatacatggccgacaaacggcatcaaggtaactcaagatccggccacaacatcgaggacgcacggcgactcgccgaccactaccagcagaacac  
cccccacccatcgccgacggggccgtgtgtcccgacaaaccactaccctgaggaccccgatccggccctgagccaaagaccccaacgcacggacgcgatcacatggctctggatgt  
gtgaccggccgggatactctcgatggacgactgttacaaggattaaagatcatgtggcattataaagatcatgtatattgttataaagatgtatgtatataatagt  
gacggccqc

**LUC7L-3xFLAG**

atgcggcccgaggcgcagatgcggccctgctggaccagactcatggcacggctggacggagacgaaaccagacagagggtaagttacagatgaccgtgtgcgaag  
agtccacccctggactgctgccccatgacatcctggctggacgcgcatggatttaggagaatgtaccaaaatccacgacttggccctccgagcagattatgagattgcaagtaa  
agaagagacctgttttgaatttagatgcaatggatcactggagtccttattgtcaatgtgatcgagaaactgagctcgcacaagaaggctggcagaacacaggagaaaa  
tcagtgcggaaagtctgcaaaggcagaaaaactgatgagttaatgaagaatagggaaaactcctgctaaagccgaacagctaggggctgaaggtaatgtggatgaaatcca  
gaagattttatggaagtggaaaaacttcgtgcgaagaaaaaagaagctgaggaagaatacagaaaattccatgcctgcattccagtttcagcagcaaaagctgcgtgtgcag  
gtctgttcagccctacccttgcattgacaatgaccgtgcctggcagaccacttcgttgcagttacacttggggctcattcagatccgagagaagctgtatcgttgaggaaaa  
ctgtcgtgaaaagcaggagaagagaaaatcaggatcgttgcaggagagagagagaggaaacgggaggcgtcagcaggaggtcggatacaaccagagatc  
caggaggtcagcgtccggatcggcgtcgaggcggtaagatcactcccgagagcgcacggaaattgtccggccggatcggatcggccaccgcag  
ccgttcccgagccacaggccgggacatcgtcgggctccgggacccaatgtgcgaaatacagaatgttccagagagcggcatccagagaggatcgttggagagcgggg  
ggagcggcggaggccccggactggaggcttgcaggatcgtccacggaggcgtcagaagagaaggaggccggcggatcgttggatataaagatcatgat  
ggcattataaagatcatgatattgattataaagatgtatgatgatataatagtgcggccgc

**LUC7L2-3xFLAG**

agaaggcaggagaaaagaaaccaggaaacggctgaaacgaagagaagagagagagagagaagaaaggagaagctgaggaggccgatcacacagaacaatccaa  
aagatccagggtccagagagcatcgacatcgatctcgctccatgcacgtgaacgcaagggagaactcgatccaaatctcgggagaaacgcacatcgccacaggcc  
ctccagcagccgtagccgcagccgtagccaccagagaagtccgtacatggagataggagcagagaacgatccaagaggagatccctaaaagaaagattcagagacc  
aagacttagcatcatgtgacagagacaggagttaagagacagatcacctcggtacagagatccgtaaagataagaagcggcttatgagatgtctaattggcagatcagaaga  
caggaggagctctgaagagcgcgaagcaggggagatccggaggggtgattataagatcatgtatggcgttataagatcatgtatattgattataaagatgtatgtatataaa  
tagtgta

### **LUC7L3-3xFLAG**

**SLC7A11-HA**

**PFKM**

### Quantitative proteomics

*LUC7L2<sup>WT</sup>* and *LUC7L2<sup>KO</sup>* cells were grown in n = 3 replicate plates in DMEM media containing 25mM glucose or galactose for 2 weeks. Quantitative proteomics was performed at the ThermoFisher for Multiplexed Proteomics (Harvard). In short, cells were harvested and total protein quantification was performed using micro-BCA assay (Pierce). Samples were reduced with DTT and alkylated with iodoacetamide before protein precipitation in methanol/chloroform. Pellets were resuspended in 200 mM EPPS, pH 8.0 and a digestion was performed sequentially using LysC (1:50) and Trypsin (1:100) based on protease to protein ratio. ~50 µg peptide per sample was labeled with TMTpro 16 reagents. A small aliquot of each sample was then combined and analyzed by LC-MS3 to verify labeling efficiency and mixing ratios. Samples were combined, desalting, and dried by speedvac. 14 fractions from the total proteome HPRP set were analyzed on an Orbitrap Eclipse mass spectrometer using a 180-minute method MS3 method with real-time search. Peptides were detected (MS1) and quantified (MS3) in the Orbitrap. Peptides were sequenced (MS2) in the ion trap. MS2 spectra were searched using the COMET algorithm against a custom protein database containing only one protein per gene (referenced as the canonical isoform). Peptide spectral matches were filtered to a 1% false discovery rate (FDR) using the target-decoy strategy combined with linear discriminant analysis. The proteins from the 14 runs were filtered to a < 1% FDR. Proteins were quantified only from peptides with a summed SN threshold of > 100. Only unique peptides were considered for downstream analysis. The mass spectrometry proteomics data have been deposited to the ProteomeXchange Consortium via the PRIDE (Perez-Riverol et al., 2019) partner repository with the dataset identifier PXD021917 and 10.6019/PXD021917.

### Next-generation RNA sequencing

Total RNA from *LUC7L2<sup>WT</sup>* and *LUC7L2<sup>KO</sup>* K562 and HeLa cells (n = 3, replicate plates each) were isolated using a RNeasy kit (-QIAGEN). RNA sequencing libraries were prepared by the Genomics Platform at the Broad Institute based on the True-Seq protocol (Illumina), which selects for polyadenylated RNA and preserves strand specificity. Libraries were sequenced using a NovaSeq 6000 instrument, generating 2x101bp paired-end reads with a minimum of 40M pairs per sample. The RNA sequencing data have been deposited to the Gene Expression Omnibus (GEO) with the dataset identifier GSE157917.

## QUANTIFICATION AND STATISTICAL ANALYSIS

Statistical tests and sample sizes are reported in the legends associated with each figure. Methods for quantification and statistical analysis of large-scale datasets are described below.

### eCLIP

Raw reads were mapped using STAR (Dobin et al., 2013) to the hg19 genome following standard ENCODE guidelines (<https://github.com/alexdobin/STAR/blob/master/doc/STARmanual.pdf>, page 9). Read length was relaxed to accommodate the slightly shorter average eCLIP read length (-outFilterMatchNminOverRead 0.33). Duplicate PCR reads were removed from the mapped reads to generate final reads. Mapped reads were then processed into peaks using CLIPper (Lovci et al., 2013) with standard specifications. For each dataset, only peaks shared between two replicates and not appearing in the input controls were considered in subsequent analyses. Reads were then filtered to a robust p value of p < 10<sup>-4</sup> or as indicated in the manuscript. Using these highest-confidence peaks, a metaplot centered on the exon was created, showing an additional 500 bases upstream and 500 bases downstream of the flanking introns. For each region (exonic or intronic), the relative positions of each single base of a CLIP peak were summed and normalized to the mean base coverage in that region.

### Gene expression

The reads were aligned with STAR (Dobin et al., 2013) to the human genome hg19 using default parameters and a two-pass approach. Following a first-pass alignment of each sample, novel splice junctions were pooled across all samples from the same cell type and incorporated into the genome annotation for a second-pass alignment. Second-pass gene counts derived from uniquely mapping pairs with the expected strandedness were output by STAR. Differential gene expression analysis between *LUC7L2<sup>WT</sup>* and *LUC7L2<sup>KO</sup>* samples was performed in R using the package DESeq2 (Love et al., 2014). Differentially-expressed genes were considered significant below FDR < 10<sup>-4</sup> and with an absolute fold change value greater than 50%.

### Splicing

Splicing events were analyzed with rMATS.4.0.2 (three replicates per condition per cell line) using standard specifications and the hg19 genome. Events were considered significant below FDR < 0.1 and with an absolute Δψ value greater than 0.05. Only events in genes with total TPM > 1 in the WT cell line of interest as called by kallisto (Bray et al., 2016) according to standard parameters were considered.

### Overlap

Overlap analyses were normalized for gene expression as in Friedman et al. (2008). Briefly, ten bins (percentiles) of gene expression were established for HeLa and K562 cells using the average gene expression from three replicates determined by kallisto (Bray et al., 2016) according to standard parameters. Averaged TPMs were filtered for TPM > 1 as above. For each bin, the percentage of genes

within that bin appearing in corresponding eCLIP or rMATS was calculated. A 10x10 matrix was then created by multiplying these frequencies together for each cell. A second 10x10 matrix was then populated by the actual counts of total overlapping genes in each cell (of 100). A third 10x10 matrix of expected counts of eCLIP/rMATS was subsequently generated from these two matrices and the total sum of this matrix represented the “expected” value of the overlap based on gene expression alone. Finally, the significance of the observed count of overlapping genes per query was estimated by Poisson (R 1.3.1093, `poisson.test`).

### Correlation

Published protein expression datasets ([Geiger et al., 2013](#); [Hutlin et al., 2010](#); [Ping et al., 2018](#); [Ubaida-Mohien et al., 2019](#)) were filtered to exclude genes with null values in > 20% of samples and remaining missing values were replaced with half the minimum observed for that protein. Each protein was normalized via Z-score and then Pearson correlations were calculated between LUC7L2 profiles and each protein. Anti-correlation with OXPHOS was assessed via a Wilcoxon Rank Sum test.

### Gene Ontology

Gene ontology analysis was performed using GOrilla with default settings and using a ranked gene list as input ([Eden et al., 2009](#)). Only GO categories with < 500 genes and represented by > 2 significant genes were considered. Highlighted genes in figures correspond to the GO categories “RNA splicing” (GO:0008380), “U1 snRNP” (GO:0005685) and “OXPHOS” (manually curated) and GO gene lists are reported in [Table S1](#).